External loops at the ferredoxin-NADP+ reductase protein-partner binding cavity contribute to substrates allocation

Ana Sánchez-Azqueta[1], Marta Martínez-Júlvez[1], Manuel Hervás[2], José A. Navarro[2], and Milagros Medina[1]

[1]*Departamento de Bioquímica y Biología Molecular y Celular, Facultad de Ciencias, and Institute of Biocomputation and Physics of Complex Systems (BIFI)-Joint Unit BIFI-IQFR (CSIC), Universidad de Zaragoza, Zaragoza, Spain.*
[2]*Instituto de Bioquímica Vegetal y Fotosíntesis, cicCartuja, Universidad de Sevilla & CSIC, Sevilla, Spain.*

Running Title: FNR external loops contribute to substrates allocation

Keywords: Ferredoxin-NADP$^+$ reductase, electron and hydride transfer, isoalloxazine:nicotinamide interaction, catalytically competent interaction, charge-transfer complex.

Correspondence to: Milagros Medina. Departamento de Bioquímica y Biología Molecular y Celular. Facultad de Ciencias. Universidad de Zaragoza. E-50009 Zaragoza. Spain. Fax +34 976 762123, Phone: +34 976 762476. E-mail: mmedina@unizar.es

Abbreviations: FNR, ferredoxin-NADP$^+$ reductase; FNR_{ox}, FNR in the fully oxidized state; FNR_{sq}, FNR in the partially reduced state; FNR_{hq}, FNR in the anionic hydroquinone (fully reduced) state; ET, electron transfer; HT, hydride transfer; WT, wild-type; CTC, charge-transfer complex; NMN, nicotinamide nucleotide moiety of NADP$^+$/H; 2'-P-AMP, 2'-P-AMP moiety of NADP$^+$/H; PPi, pyrophosphate; k_{HT}, k_{HT-1}, hydride transfer first-order rate constants for the forward and reverse reactions, respectively; k_{et}, electron transfer rate constant.

Acknowledgements: This work has been supported by MINECO, Spain (Grant BIO2010-14983 to M.M) and the Andalusian Government-FEDER (PAIDI BIO-022 to J.A.N.). A. S-A holds a FPU fellowship from the Spanish Ministry of Education.

Summary

Ferredoxin-$NADP^+$ reductase (FNR) is the structural prototype of a family of FAD-containing reductases that catalyze electron transfer between low potential proteins and $NAD(P)^+/H$, and that display a two-domain arrangement with an open cavity at their interface. The inner part of this cavity accommodates the reacting atoms during catalysis. Loops at its edge are highly conserved among plastidic FNRs, suggesting they might contribute to both flavin stabilization and competent disposition of substrates. Here we pay attention to two of these loops in *Anabaena* FNR. The first is a sheet-loop-sheet motif, $loop_{102-114}$, that allocates the FAD adenosine. It was thought to determine the extended FAD conformation, and, indirectly, to modulate isoalloxazine electronic properties, partners binding, catalytic efficiency and even coenzyme specificity. The second, $loop_{261-269}$, contains key residues for the allocation of partners and coenzyme, including two glutamates, Glu267 and Glu268, proposed as candidates to facilitate the key displacement of the C-terminal tyrosine (Tyr303) from its stacking against the isoalloxazine ring during the catalytic cycle. Our data indicate that the main function of $loop_{102-114}$ is to provide the inter-domain cavity with flexibility to accommodate protein partners and to guide the coenzyme to the catalytic site, while the extended conformation of FAD must be induced by other protein determinants. Glu267 and Glu268 appear to assist the conformational changes that occur in the $loop_{261-269}$ during productive coenzyme binding, but their contribution to Tyr303 displacement is minor than expected. Additionally, $loop_{261-269}$ appears a determinant to ensure reversibility in photosynthetic FNRs.

Introduction

Ferredoxin-$NADP^+$ reductases (FNR) from photosynthetic organisms catalyze the production of NADPH in plants and cyanobacteria [1-3]. Their mechanisms are well characterized and they are the structural prototype for a large family of flavin-dependent oxido-reductases that participate in several biological reactions such as nitrogen fixation, steroid metabolism, iron-sulfur cluster biogenesis and oxidative-stress response [4, 5]. Nevertheless, recent studies have indicated that additional residues to those directly implicated in the catalytic event, might also have an important contribution at the molecular level to the enzyme functionality [3, 6-10]. Members of the family share the presence of a basic module consisting on a flavin-binding domain (FAD or FMN) and a pyridine nucleotide-binding domain ($NAD(P)^+/H$) [11]. Generally, the cavity at the interface between the two domains contains the electron carrier protein partner (ferredoxin (Fd) or flavodoxin (Fld)) binding site. Affinity and stability of the FNR complexes with its partners are mainly defined by direct contacts through their binding regions, but structural views indicate that more distant protein regions might also contribute to the overall process (**Figure SM1**) [3, 12, 13].

Structural comparison of some FNR-like representatives indicates differences in the conformation of their FAD cofactors (**Figure 1A**). In plastidic-type FNRs the FAD is held in a L-shaped extended conformation, where the PPi group acts as a hinge and the adenosine moiety is bound to a flexible sheet-loop-sheet motif ($loop_{102-114}$ in *Anabaena* FNR (*An*FNR)) where particular interactions are produced among the adenosine of FAD and the Tyr104 side-chain (including π-π stacking and a H-bond between the adenosine O4 atom and the Tyr104 hydroxyl) [14-16]. In NAD-dependent proteins of the same structural family, such as nitrate reductases (NR) or cytochrome b_5 reductases (Cb5R), as well as in FNRs from proteobacteria, FAD shows different folded conformations [17-20]: for example, in rat Cb5R (*r*Cb5R) the adenosine folds back, and sandwiched between a Tyr and a Phe (**Figures 1A and 1C**). Moreover, the catalytic efficiencies of bacterial FNR homologues and of NAD-dependent reductases, as well as their midpoint reduction potentials, differ from those of plastidic FNRs, inferring some relationship between these properties and the flavin conformation.

Electron (ET) and hydride (HT) transfer steps involving $FNR_{hq/ox}$ and $NADP^+/H$ or $Fd_{ox/rd}/Fld_{sq/hq}$ are in general very fast processes, in which the enzyme specifically recognizes its partners and brings the reacting atoms into an optimal geometry [3, 12, 21-25]. During HT between $FNR_{hq/ox}$ and $NADP^+/H$, the specific recognition of the phosphorylated pyridine nucleotide is guaranteed by the presence of a bipartite binding site in the enzyme that maintains inaccessible the binding cavity for the reactive nicotinamide nucleotide portion of $NADP^+/H$ (NMN) until accommodating its 2'P-AMP moiety [26, 27]. On the contrary, in NAD-dependent members of the family, the NAD-binding region consists of a preformed cavity able to accommodate the whole nucleotide without any protein re-arrangement [19, 28-30]. Replacements in the 2'-P-AMP and PPi binding regions of several FNRs have only provided minor improvements in modulating coenzyme specificity, with the only exception of the FNR from *Plasmodium falciparum* [31-35]. However, improvements in affinity for NAD^+/H were reported when remodeling the $NADP^+/H$ binding cavity to create a preformed site, but these complexes were unproductive since the NMN moiety did not reach the active site [33]. This last step of the competent placement of the NMN moiety against the isoalloxazine relies on the displacement of the C-terminal tyrosine side-chain (Tyr303 in *An*FNR). The exact forces and mechanism driving that movement still remain unknown [7, 36-38], but crystallographic data and molecular dynamic (MD) simulations pointed to a possible regulatory role played by Arg264. Its guanidinium has been detected adopting two main conformations: one interacting with the carboxylates of Glu267 and Glu268, and the other one connecting the Tyr303 terminal carboxylate (**Figure 1B** and see **Figure 4** from [39]) [14, 22, 39].

In the present work, we gain further information about the particular roles of the above mentioned regions. Guided by sequence and structure alignments, we produced and characterized a single mutant, Y104F, and a multiple mutant, E103Y/Y104F/S109F/G110P, in $loop_{102-114}$ of *An*FNR with the aim to mimic an environment that would induce a folded FAD conformation. On the other hand, the E267A/E268M *An*FNR double mutant was conceived to prevent interactions of these residues with Arg264 during the catalytic event. The binding and catalytic properties of the three *An*FNR variants, as well as their abilities for ET and HT, respectively, with Fd and $NAD(P)^+/H$, are here reported, giving further clues about their roles in substrate recognition and NMN competent entrance into the active site.

Materials and methods

Biological material

The pET28a:*An*FNR plasmids containing the Y104F, E103Y/Y104F/S109F/G110P and E267A/E268M mutations were obtained from the company Mutagenex® and used to produce the corresponding proteins from *E. coli* cultures, which were purified as previously reported [32]. *Anabaena* Fd (*An*Fd) was produced as previously described [24]. Protein samples were dialyzed in 50 mM Tris/HCl, pH 8.0 and concentrated using Amicon Ultra-15® centrifugal filters with a 10000 Dalton or a 5000 Dalton pore size for FNR or Fd, respectively. Protein preparations were made anaerobic by successive cycles of air evacuation and flushing with O_2-free Ar in 50 mM Tris/HCl, pH 8.0. FNR_{hq} variants were obtained by anaerobic photoreduction of the samples in the presence of 2 μM 5-deazariboflavin (dRf) and 3 mM EDTA in 50 mM Tris/HCl, pH 8.0 by irradiation from a 250 W light source [23].

Spectrocopic assays

Uv-Vis spectra were recorded in a Cary-100 spectrophotometer. The molar absorption coefficient for each FNR variant was spectrophotometrically determined by thermal denaturation of the protein for 10 min at 90ºC, followed by centrifugation and separation of the precipitated apoprotein, and spectroscopic quantification of the FAD released to the supernatant [40]. Photoreduction and potentiometric titrations were attempted in the presence of dRf/EDTA as previously reported [24]. These are long-lasting measurements where protein samples are illuminated and let under agitation at 25ºC, therefore, the low stability of the FNR mutants here studied prevented their full characterization. Interaction parameters with $NADP^+$ and NAD^+ were determined by difference absorption spectroscopy at 25ºC in 50 mM Tris/HCl, pH 8.0 as previously described [31]. Errors for the K_d and Δε values were ± 10% and ± 5%, respectively.

Steady-state kinetics measurements

The diaphorase activity of the FNR mutants was assayed in a double beam Cary-100 spectrophotometer using 2,6-dichlorophenolindophenol (DCPIP) ($\Delta\varepsilon_{620nm}$ 21 $mM^{-1}.cm^{-1}$) or $K_3Fe(CN)_6$ ($\Delta\varepsilon_{420nm}$ 1.05 $mM^{-1}.cm^{-1}$) as two- or one-electron acceptors,

respectively, and NADPH or NADH as electron donors. All measurements were carried out in 50 mM Tris/HCl, pH 8.0 at 25ºC. The final reaction mixture contained 4 nM FNR, either 0.1 mM DCPIP or 1.5 mM $K_3Fe(CN)_6$, and NADPH in the range 0-200 µM, or 1 µM FNR and higher nucleotide concentrations (0-5 mM) when assayed with NADH, while the reference cuvette contained 0.06 mM DCPIP when using this acceptor. The NADPH-dependent cytochrome *c* (Cyt*c*) reductase activity was determined using recombinant *An*Fd, and horse heart Cyt*c* as final electron acceptor. Reaction mixtures contained 4 nM FNR, 200 µM NADPH, 0.75 mg/ml Cyt*c* and 0-15 µM *An*Fd. Kinetic results were analyzed using a Michaelis-Menten model, and K_m and k_{cat} values were obtained by fitting the dependence of the observed initial rates on coenzyme concentration to this equation. Estimated errors in K_m and k_{cat} were ± 10% and ± 5%, respectively, for the diaphorase measurements, and ± 20 % for the Cyt*c* activity.

Laser-flash induced kinetics

Time resolved ET reactions from *An*Fd_{rd} to WT and E103Y/Y104F/S109F/G110P FNR_{ox} were measured using laser-flash photolysis at 25ºC under anaerobic conditions in a 1 cm path-length cuvette, using EDTA as electron donor and dRf as photosensitizer, as previously described [41]. The standard reaction mixture contained, in a final volume of 1.5 mL, 4 mM sodium phosphate, pH 7.0, 1 mM EDTA and 100 µM dRf, in the presence (standard buffer) or the absence (low ionic strength (*I*) buffer) of 100 mM NaCl. Direct reduction of *An*FNR_{ox} by the laser-flash generated dRf semiquinone (dRfH•) was followed by measuring the decrease of absorbance at 458 nm. When both Fd in excess (40 µM) and FNR are present simultaneously in the solution, the subsequent ET process from the generated Fd_{rd} to FNR_{ox} can be monitored as the increase of absorbance at 600 nm due to the production of FNR_{sq} [10, 13, 23, 24]. Control experiments collected at 489-500 nm, an isosbestic point of the $FNR_{ox/sq}$ couple, allowed monitoring the oxidation of Fd_{rd}, yielding rate constants that were the same, within experimental error, as those determined from the 600 nm data. The effect of the ionic strength in the reaction was analyzed by adding aliquots of a 5 M NaCl solution to a reaction cuvette containing 40 µM *An*Fd and 30 µM *An*FNR in low *I* buffer. All experiments were performed under pseudo-first-order conditions, for which the amount of acceptor (FNR_{ox}) was maintained well in excess

over the amount of the generated Fd_{rd} (<1 μM). Each kinetic trace was the average of 8-15 measurements. All kinetic traces were fitted to monoexponential curves by using the Marquardt method to obtain the pseudo-first observed rate constants (k_{obs}). Non-linear k_{obs} dependences on FNR concentration were adjusted to a two-step mechanism [23, 42],

$$Fd_{rd} + FNR_{ox} \underset{k_{-1}}{\overset{k_1}{\rightleftharpoons}} [Fd_{rd}{:}FNR_{ox}] \overset{k_{et}}{\rightarrow} Fd_{ox} + FNR_{sq}$$

to estimate minimal values of both the forward association (k_1) and reverse dissociation (k_{-1}) rate constants, as well as the equilibrium dissociation constant ($K_d = k_{-1}/k_1$) and the ET rate constant (k_{et}). Errors in the estimated values of K_d and k_{et} were ± 20% and ± 10%, respectively.

Stopped-flow pre-steady-state kinetic measurements

Fast HT processes between the $FNR_{hq/ox}$ variants and $NADP^+$/H, as well as between E267A/E268M $FNR_{hq/ox}$ and NAD^+/H were followed by stopped-flow using an *Applied Photophysics* SX17.MV equipment with a photodiode array detector. Measurements were carried out in 50 mM Tris/HCl, pH 8.0 at 6ºC under anaerobic conditions as previously described [8, 21]. Final FNR concentrations were 25 μM, while a 25-250 μM range was used for the nucleotide. Absorption spectra (400-1000 nm) were collected every 2.5 ms and processed using the X-Scan software (*App. Photo. Ltd.*). Analysis of time dependent spectral changes was performed by global analysis and numerical integration methods using Pro-Kineticist (*App. Photo. Ltd.*). The observed conversion rate constants ($k_{A\rightarrow B}$, $k_{B\rightarrow C}$) were calculated by fitting the collected data to a single step model. In most cases, a previous reaction (A→B) had occurred within the instrumental death time, leading to charge transfer complex (CTC) formation. In those cases we correlate the measurable reaction to a B→C model, being B and C spectral species reflecting a distribution of enzyme intermediates (reactants, CTCs, products, Michaelis complexes) at a certain point along the reaction time course, and not necessarily a single distinct enzyme intermediate. Model validity was assessed by lack of systematic deviations from residual plots at different wavelengths, inspection of calculated spectra and consistence among the number of significant singular values with the fitting model. In general, no dependence profiles on the $NADP^+$/H concentration

were observed for the HT processes analyzed, probably due to the reversibility of the processes and the maximal $k_{B\rightarrow C}$ values were obtained at the 1:1. Since it was not possible to determine reduction midpoint potentials for the mutants here analyzed we were not able to globally fit the apparent rate constants as a function of coenzyme concentration to the sum of the rates for the forward (k_{HT}) and reverse (k_{HT-1}) HT at equilibrium [22, 43]. Therefore, as accepted in similar cases [8, 21], we related $k_{B\rightarrow C}$ with the maximal experimental HT rate constant, k_{HT} or k_{HT-1}, values. For the reduction of E267A/E268M FNR, $k_{A\rightarrow B}$ derived from experimental data showed a dependence profile on the NADPH concentration fitting to the equation describing binding at a single site followed by the HT process,

$$k_{A\rightarrow B} = \frac{k_{HT-1}(K_d+/NADPH)+k_{HT}[NADPH]}{[NADPH]+K_d}$$

and allowed the determination of K_d and k_{HT} values. Errors in the estimated values of K_d and k_{HT} values were ± 20% and ± 15%, respectively, while those of $k_{A\rightarrow B}$ or $k_{B\rightarrow C}$ were ± 10%.

Crystal growth, data collection and structure refinement

The E103Y/Y104F/S109F/G110P variant of *An*FNR was crystallized under same conditions as those reported for WT FNR [27]. X-ray data set was collected in the ID23-1 line at ESRF (Grenoble, France) and processed with XDS [44] and SCALA from CCP4 [45]. The first model was obtained by MOLREP [46] from CCP4, using the WT FNR structure (1QUE) as template. Refinement of the structure was performed with Refmac5 [47] from CCP4, alternating with manual model building with COOT [48]. PROCHECK [49] and MOLPROBITY [50] programs were used to assess final structure. A single crystal of E103Y/Y104F/S109F/G110P FNR diffracted up to 1.70 Å and belonged to the $P6_5$ hexagonal space group. Its V_m was 2.95 $Å^3$/Da with one FNR molecule in the asymmetric unit and 58.4 % solvent content. The model comprised residues 9-303, one FAD molecule, one SO_4^{2-} ion, one glycerol molecule and water molecules. Data for collection and refinement processes can be found in Table SP1. The coordinates and structure factors for this FNR variant have been deposited with PDB ID: 4C43.

Results

Spectral properties of the FNR_{ox} variants and interaction with the coenzyme

The level of expression in *E. coli* of all the FNR mutants was similar to that of WT, and purification yielded well-folded and FAD assembled FNRs. The mutants showed similar spectral properties to WT *An*FNR_{ox}, with absorbance maxima of the flavin band-I at 458 nm and extinction coefficients at this wavelength not varying significantly, indicating no major structural perturbations in the close environment of the FAD isoalloxazine ring. However, Y104F FNR suffered some loss of the FAD cofactor when dialyzed, and E267A/E268M FNR was not soluble at concentrations over 60 μM. Moreover, stepwise photoreduction of Y104F, E103Y/Y104F/S109F/G110P and E267A/E268M FNRs induced FAD dissociation and protein denaturation, preventing determination of their midpoint reduction potentials. These observations indicate that the mutations particularly affect the strength of the ApoFNR:FAD_{hq} complex, suggesting weakening of the affinity for the reduced form of the cofactor.

Difference spectra obtained upon titration of Y104F, E103Y/Y104F/S109F/G110P and E267A/E268M FNRs with $NADP^+$ were similar to those for the WT protein, with only minor displacements of the positions of minima and maxima (**Figure 2**). The hyperbolic dependence of the absorbance changes upon increasing $NADP^+$ concentrations allowed determination of K_d^{NADP+} as well as of the magnitude of the change upon complex formation, Δε (**Table 1**). K_d^{NADP+} did not vary significantly either being just slightly smaller, 1.5-fold for the Y104F and E103Y/Y104F/S109F/G110P FNRs, or up to 3.3-fold for E267A/E268M FNR. Therefore while the $loop_{102-114}$ appears to have minor effects on $NADP^+$ binding, the glutamates in positions 267 and/or 268 in the WT enzyme appear contributing to reduce the affinity for this form of the coenzyme. Titration of all FNR variants with NAD^+ did not induce any difference spectra, indicating that this coenzyme was not able to produce changes in the flavin environment. This suggests that its nicotinamide ring is not bound in the enzyme flavin environment.

Steady-state kinetic parameters of the FNR mutants

Either DCPIP or potassium ferricyanide, as final artificial two- or one- electron acceptors respectively, were used to obtain the diaphorase steady-state kinetic parameters of the FNR variants (**Table 1**). Y104F and E103Y/Y104F/S109F/G110P

FNRs displayed behaviors very similar to that of WT, though in general k_{cat} values slightly decreased. Regarding E267A/E268M FNR, k_{cat} values were also slightly lower and K_m^{NADPH} values were within 2-fold of those of the WT: increasing when using ferricyanide as electron acceptor and decreasing when using DPCIP. Therefore, the E267A/E268M FNR catalytic efficiency increased around 2-fold when using a two-electron acceptor, while decreased in a similar range when using a one-electron acceptor. Finally, the diaphorase activity of E267A/E268M FNR showed a remarkable k_{cat} increase regarding WT FNR when using NADH as electron donor. As consequence, this variant was two orders of magnitude less specific for NADPH *versus* NADH than the WT.

The introduced mutations produced more important deleterious effects in the Fd mediated NADPH dependent Cyt*c* reductase activity of FNR (**Table 2)**. Despite E103Y/Y104F/S109F/G110P FNR exhibited a similar behavior to the WT in terms of k_{cat}, this parameter resulted reduced by 8- and 2.5-fold for Y104F and E267A/E268M FNRs, respectively. Moreover, K_m^{Fd} increased for all the variants, but particularly for those at $loop_{102-114}$, suggesting that the mutations reduce the affinity of FNR for Fd, at least in an optimal orientation for ET. All together these parameters indicate that the introduced mutations, but particularly the single replacement of Tyr104 by Phe, have an important negative impact in the non-photosynthetic ET from FNR to Fd.

Transient kinetics for ET from Fd to FNR

The low stability of Y104F and E267A/E268M FNRs prevented their characterization by laser-flash spectroscopy. However, direct reduction of the E103Y/Y104F/S109F/G110P FNR isoalloxazine to its neutral semiquinone form by the laser-flash generated dRfH• could be followed by a decrease of the absorption at 458 nm following a monoexponential decay, as observed for the WT FNR [23]. k_{obs} values resulted linearly dependent on the FNR concentration and allowed obtaining second-order bimolecular rate constants (k_2) of the same order of magnitude as for the WT (**Table 3**) [23]. This observation indicated that this mutant is as efficiently reduced by dRfH• as WT.

In the presence of an excess of Fd_{ox}, the laser-generated dRfH• causes the initial fast reduction of this protein, followed by a subsequent ET step from Fd_{rd} to FNR_{ox}, that

can be monitored by an absorption increase at 600 nm due to formation of the neutral FNR_{sq} [23, 24]. Reduction of FNR_{ox} by Fd_{rd} has been here investigated in the presence of a moderately high salt concentration (I = 120 mM), conditions reported as optimal for this ET reaction [23]. Moreover, k_{obs} values presented a hyperbolic dependence on enzyme concentration that can be related with the formation of a transient FNR_{ox}:Fd_{rd} complex prior to the ET step (**Figure 3A**) [51]. The two-step model here applied to estimate K_d and k_{et} values has largely demonstrated to be useful in the characterization of ET in transient protein:protein reactions [10, 13, 41, 42, 52]. The model is based in the total amount of FNR_{ox} in the sample as it is widely accepted that, in transient protein complexes, protein association/dissociation is much faster than ET itself, and thus the ET process would be the rate limiting step rather than protein exchange. Thus, applying the formalism previously described [42], minimal values for k_{et}, k_1 and k_{-1} (and K_d) could be estimated (**Table 3**). These values suggested a 4-fold decrease in the affinity of the Fd:FNR complex induced by the introduced mutations, whereas the ET process remains basically unaffected.

The influence of I was further analyzed to investigate the effects induced by the combined E103Y/Y104F/S109F/G110P mutations on the Fd:FNR interaction. As reported for the WT, biphasic dependences of k_{obs} with increasing I were also observed for the variant (**Figure 3B**). The bell-shaped profile for the dependence of k_{obs} with I is related with the re-arrangement of the initial FNR_{ox}:Fd_{rd} encounter transient complex to achieve an optimal ET conformation, indicating the occurrence of protein-protein dynamic motions that are blocked by strong electrostatic interactions at very low I [23]. However, the k_{obs} maximum was shifted to higher I for the mutant, suggesting the occurrence of stronger electrostatic interactions in the encounter complex than in the WT system.

Transient kinetics of the hydride transfer reactions

Fast HT processes between WT *An*$FNR_{hq/ox}$ and $NADP^+$/H occur through the formation of two intermediate CTCs [21, 22]: [FNR_{ox}-NADPH] (CTC-1, characterized by an absorbance spectral band with maximum at ~ 600 nm), and [FNR_{hq}-$NADP^+$] (CTC-2, showing a broad band centered at ~ 800 nm). The HT event occurs in the transition of CTC-1 to CTC-2, or *viceversa*. Similarly to the WT, reduction of Y104F, E103Y/Y104F/S109F/G110P and E267A/E268M *An*FNR_{ox}s by NADPH showed CTC-

1 formation and protein reduction (measurable by the decrease of the flavin band-I absorbance at 458 nm) in the instrumental death time, with subsequent spectral evolution including additional reduction of the enzyme and formation of CTC-2 (**Figures 4A-4D**). This multiple wavelength spectral evolution best fitted to a single-step model that includes the HT event, and thus the observed rate constants are named $k_{B\rightarrow C}$. For the Y104F and E103Y/Y104F/S109F/G110P variants, $k_{B\rightarrow C}$ values were independent on the NADPH concentration as in the WT, being, therefore, related with limiting k_{HT} values (**Table 4**). However, a concentration dependence hyperbolic profile was observed for the E267A/E268M FNR process allowing determination of a K_d^{NADPH} value that suggested a weaker FNR:NADPH interaction than in WT (**Table 4**). Nevertheless, significant negative effects on k_{HT} were not observed in any of the mutants.

Y104F and E103Y/Y104F/S109F/G110P FNRs also behaved very similar to WT *An*FNR when assaying the reverse reaction. Thus, reduction of $NADP^+$ by these FNR_{hq} variants showed appearance of a small amount of CTC-2 concomitant with mild protein reoxidation within the instrumental dead time, followed by subsequent spectral evolution including flavin oxidation and CTC-1 formation (**Figures 4E-4G**). Kinetic parameters for these processes were also similar to those of WT (**Table 4**). On the contrary, HT from E267A/E268M FNR_{hq} to $NADP^+$ occurred with minor CTC stabilization (**Figure 4H**), particularly of CTC-2, and with a 2-fold decrease in k_{HT-1}.

HT processes for E267A/E268M FNR were also assayed with the non-phosphorylated pyridine nucleotide, NAD^+/H, to determine if the augmented steady-state catalytic efficiency observed for this variant with NADH might be a consequence of a more efficient HT reaction. Similarly to that reported for the WT, reactions between E267A/E268M FNR and NAD^+/H were extremely slow processes that did not lead to CTC stabilization (not shown) [33]. Nevertheless, comparison of rate constants for WT and E267A/E268M FNRs using a 1:5 protein:NAD^+/H ratio, led to a slight increase in the apparent HT rate contants by the introduced mutations ($k_{A\rightarrow B}^{WT}$ = 0.02 s^{-1} and $k_{A\rightarrow B}^{E267A/E268M}$ = 0.08 s^{-1} for the reduction by NADH and $k_{A\rightarrow B}^{WT}$= 0.1 s^{-1} and $k_{A\rightarrow B}^{E267A/E268M}$ = 0.8 s^{-1} for oxidation by NAD^+).

The structural environment of the mutated positions

The overall folding of E103Y/Y104F/S109F/G110P *An*FNR is pretty similar to that of WT *An*FNR (0.73 Å for 295 Cα atoms aligned). Poor electron density did not allow determining the position of residues 106 and 107. However residues flanking them, including the mutated ones, show a good density that allows describing the peptide chain in this region. Mutations on the adenosine binding loop did not lead to a remarkable change in the overall positioning of FAD that keeps extended conformation with only its adenosine moiety differing somehow in conformation regarding to the WT structure (**Figure 5**). The absence of the Tyr104 hydroxyl, in the WT FNR H-bonding the ribose O4 atom (**Figure 5B**), is compensated by an intramolecular H-bond between both adenosine O4 and N3 atoms that seems to force a twist and a slight displacement of the adenosine moiety (**Figure 5C**). On the other hand and due to the introduced mutations, the loop shows a more open conformation than in the WT structure. So, in the mutant the $loop_{102\text{-}114}$ points outwards and differs from its WT conformation with an r.m.s.d. of 4.18 Å. Another significant structural feature observed in the mutant structure concerns to the conformation of the Arg264 side-chain (**Figure 5**). As already described in other *An*FNR structures [9, 22], its guanidinium group moves, in this mutant 5 Å, towards the Tyr303 carboxylate. This observation reinforces the idea of differently populated orientations of this Arg side-chain in position during coenzyme binding and catalysis.

Discussion

The sheet-loop-sheet motif ($loop_{102\text{-}114}$ in AnFNR) binding the FAD adenosine in plastidic FNRs

Comparison of plastidic FNRs with NAD-dependent members of the family (**Figures 1A** and **1C**) drove us to the production of two variants in the FAD adenosine binding $loop_{102\text{-}114}$: Y104F and E103Y/Y104F/S109F/G110P FNRs. The Y104F mutant was intended to disrupt the H-bond between the Tyr104-OH and the FAD adenosine, while keeping the stacking interaction with the aromatic side-chain. On the other hand, the E103Y/Y104F/S109F/G110P one was expected to induce a change in the orientation of $loop_{102\text{-}114}$ towards that displayed by some NADH-dependent members of the family (**Figure 1A**). However, the crystal structure of E103Y/Y104F/S109F/G110P FNR resulted practically identical to that of the WT protein, with the FAD in an extended conformation very similar to the WT enzyme (**Figure 5**). Moreover, the inherent flexibility of $loop_{102\text{-}114}$ and of the FAD adenosine moiety in plastidic FNRs [27, 39] is

even enhanced in the mutant. This might counteract changes in the shape of the flavin binding site introduced by the mutations. Similarly, an unaltered FAD conformation has been observed in two engineered pea and *E. coli* FNRs (plastidic- and bacterial-type FNRs, respectively) upon deletion and insertion, respectively, of the plastidic characteristic adenosine binding strand-loop-strand motif [53]. Therefore, the binding and kinetic effects induced by these mutations in *An*FNR must account mainly for changes in the nature of their side-chains rather than to the expected alterations on FAD conformation. In *An*FNR, most of the protein connections with the ribose and adenine moieties of FAD are bridged by water molecules, and only one direct H-bond is established with Tyr104-OH. Disruption of this connection in the Y104F mutant appears to have an important impact in FAD affinity, particularly in its reduced state. However, the lack of stability of this variant was recovered upon introduction of the three additional mutations in E103Y/Y104F/S109F/G110P FNR, where, although the WT contact between the FAD and the loop was still missing, a new FAD intramolecular H-bond between both adenosine O4 and N3 atoms forces a twist in the adenine orientation a the displacement of this adenosine moiety (**Figure 5**).

Apart from weaker FAD binding, substitutions in the $loop_{102\text{-}114}$ did not lead to mayor changes on FNR overall folding, nor in its $NAD(P)^+$/H binding and catalytic parameters (**Tables 1** and **4**). Nevertheless, deleterious effects were particularly observed in the affinity for the protein partner, with minor effects on ET rates (k_{et} and k_{cat}) (**Tables 1, 2** and **3**). This might be related with the clear retraction observed in the position of the $loop_{102\text{-}114}$ upon introduction of the mutations regarding those in free WT FNR and in the Fd:FNR comples, which appears having a negative effect in the initial recognition event between partners (**Figure SM2**). All together these data suggest that the main function of the $loop_{102\text{-}114}$ is to provide flexibility to the inter-domain cavity to assits guiding of the coenzyme and, particularly, of the protein partners and to their binding cavities, while other structural determinants will be responsible for the FAD extended conformation.

Role of $loop_{261\text{-}269}$ in AnFNR in the competent binding of substrates

The simultaneous substitutions of Glu267 and Glu268 in *An*FNR also affected the affinity for the protein partner (**Table 1**). The crystal structure of the *An*Fd:*An*FNR complex situates Arg264 and Glu267 at the complex interface, H-bonding Fd-

Tyr25/Arg42, and Asp62, respectively (**Figure SM3**) [13, 25, 54]. E267A/E268M FNR eliminates two negative charges on the FNR surface, as well as the possibility of H-bonding at position 267, and, conceivably the displacement of the native Arg264 arrangement might be possible. Therefore, both the initial interaction governed by electrostatic attractive forces and the subsequent optimal complex surface adjustment would be affected, thus explaining the increase on K_d^{Fd} and the decrease on k_{cat} observed for the Cyt*c* reductase activity (**Table 2**), and also in agreement with previously reported deleterious effects for the D62K *An*Fd mutant [55]. Additionally, the midpoint reduction potential appears altered in the mutant, making ET to Fd less favorable. Binding and HT data for E267A/E268M FNR with the coenzyme are indicative of higher FNR_{ox}:$NADP^+$ and lower FNR_{ox}:NADPH affinities, but with final catalytic geometries optimal and non-optimal for FNR_{ox}:NADPH and FNR_{hq}:$NADP^+$, respectively (**Tables 1** and **4**). Therefore, a role must be accepted for these two residues in coenzyme accommodation during catalysis, and in ensuring the reaction is able to take place either in the photosynthetic or non-photosynthetic directions as required by the organism, a particular feature of plastidic FNRs. This is in agreement with $loop_{261-269}$ being a determinant for competent $NADP^+$/H recognition and NMN allocation [8, 32, 33]. Thus, $loop_{261-269}$ undergoes several conformational changes during the proposed three-step (WT→C-I→C-II→C-III) $NADP^+$/H binding process [27], which involve changes in the conformation of Arg264 and Glu267 side-chains and in the interactions they establish along the transitions (**Figure 6A**). In WT and C-I, the C-terminal Tyr303 carboxylate and the Thr302-OH are situated at H-bond distance of the Arg264 amide and the Glu267 carboxylate, respectively. The transition of C-I into C-II (**Figure 6A to Figure 6B**) entails displacement of $loop_{261-269}$ and rotation of the Leu263 side-chain to accommodate the PPi and NMN moieties, breaking Arg264-Tyr303 and Glu267-Thr302 H-bonds. Finally, allocation of the NMN moiety into the active site in C-III (represented by the structure of the Y303S FNR:$NADP^+$ complex) appears accompanied by partial return of $loop_{261-269}$ to its original position (**Figure 6C**). Thus, the C-ter-$loop_{261-269}$ connections must first break apart to allow Leu263 displacement, and then get restored to assist Tyr303 displacement; two steps crucial for competent coenzyme binding. The low E267A/E268M FNR stability prevented its crystallization, but we constructed its structural model. This model suggested a displacement of $loop_{261-269}$ with respect to the original template structure, and resembled that of the C-II complex (**Figure 6B**), reinforcing the proposed influence of a Glu267-Thr302 bond in positioning of $loop_{261-}$

$_{269}$ regarding Tyr303. This conformation can explain both the higher E267A/E268M FNR_{ox}:$NADP^+$ affinity and the enhanced NADH activity due to nucleotide entrance resulting less blocked by the side-chain of Leu263, thus making 2´-AMP recognition less critical for optimal coenzyme binding (**Table 1**). Displacement of Tyr303 is hence proposed as consequence of additive forces that all together compensate for the disruption of π-π stacking and H-bond interactions with Ser80 and Glu301: the nicotinamide ring pushes Tyr303 from one side while the $loop_{261-269}$ pulls from the other. Additional concerted roles played by other protein regions are not discarded. Among them, the movement of Glu301 and the loss of its H-bond connection with Tyr303-OH [56] and the assistance by Fd binding [57, 58] may be especially relevant. According to E267A/E268M FNR k_{HT} and k_{HT-1} values (**Table 4**), contribution of $loop_{261-269}$ to Tyr303 displacement appears to be more important in the photosynthetic HT reaction, while the pushing effect of the nicotinamide would dominate the backward process. MD simulations further support this hypothesis [39]. Similarly, the HT reaction from a FNR_{hq} mutant previously produced at Arg264, R264E, to $NADP^+$ resulted slightly slowed down compared to WT, while k_{HT} values remained unaltered [25]. The different effects observed depending on the HT direction might be also related to divergences in the sequences of the $loop_{261-269}$ among plant-type reductases (**Figure 1C**). Glu267 is conserved among photosynthetic FNRs and the presence of a glutamate in the following position is characteristic of some cyanobacterial enzymes, while higher plants have a Lys and a non-polar side-chain is found in the position equivalent to Thr302. The characteristic Glu-Lys pair of leaf FNRs is replaced by a Met-Pro one in FNRs from plant roots and other non-photosynthetic organisms, such as *Leptospira interrogans* FNR. This, together with observed differences in residues at positions equivalent to $loop_{261-269}$ and NMN occupancy upon $NADP^+$ binding may be related to the preferential direction of their physiologically catalyzed reactions [11, 15, 59-61]. Thus, $loop_{261-269}$ might contain the determinants for the reversibility of the HT process in photosynthetic FNRs.

In conclusion, the *An*FNR mutants here analyzed on the FAD adenosine and $NADP^+$ binding loops further confirm the complexity of the mechanisms addressing oxido-reduction partner selectivity and catalytic efficiency in these reductases, in agreement with previous unsuccessful attempts to re-design FNRs with modified binding and/or HT properties. The results here presented conclude that the flexibility of

loop$_{102\text{-}114}$ allows a competent final relative distance of the redox catalytic centers, particularly modulating Fd binding and ET. Additionally, direct interactions between the side-chain of Arg264 and those of Glu267 and Glu268 do not play a crucial role in Tyr303 displacement, though all they participate in the $NADP^+$/H binding processes by assisting the conformational changes that occur in the loop$_{261\text{-}269}$ during productive coenzyme binding as well as to the reversibility of the HT process.

Figure Legends

Figure 1. Conformation of the FAD cofactor in the FNR family. (A) Superposition of crystal structures of *An*FNR (PDB ID: 1QUE, in green) and rat Cb5R (PDB ID: 1I7P, in purple). Residues stacking the isoalloxazine and adenosine rings of FAD are shown as sticks. The inset shows a detail of the environment of the FAD adenosine moiety, stacked between Tyr112 and Phe120 in rat Cb5R and connected through H-bond and stacking interactions with Tyr104 in *An*FNR. **(B)** Conformations of Arg264, Glu267 and Glu268 in *An*FNR (PDB ID: 1QUE, in green), in a *An*FNR:$NADP^+$ complex (PDB ID: 1GJR (known as C-II), in blue) and in Y303F *An*FNR (PDB ID: 2X3U, in yellow). **(C)** Sequence alignment of different NADP- and NAD-dependent members of the FNR superfamily (ClustalW2). Positions analyzed in this work are highlighted in green, numbers on the top correspond to the *An*FNR numbering.

Figure 2. Interaction of the FNR mutants with the coenzyme. Difference absorbance spectra elicited upon titration of WT (──), E103Y/Y104F/S109F/G110P (····) and E267A/E268M (---) FNRs (~ 20 μM) with saturating concentrations of $NADP^+$ in 50 mM Tris/HCl, pH 8.0 and 25ºC.

Figure 3. Transient ET from Fd_{rd} to E103Y/Y104F/S109F/G110P FNR_{ox}. (A) Dependence on FNR_{ox} concentration of the observed rate constants (k_{obs}) for the reduction by Fd_{rd} of WT (●) and E103Y/Y104F/S109F/G110P (■) FNR at I = 120 mM. Reaction mixtures contained 40 μM Fd_{ox}. **(B)** Dependence on the square root of I of k_{obs} for the reduction of WT (●) and E103Y/Y104F/S109F/G110P (■) FNR_{ox} by Fd_{rd}. Samples contained 30 μM FNR_{ox} and 40 μM Fd_{ox}. Reactions were carried out in 4 mM phosphate, pH 7.0 and 25ºC.

Figure 4. Transient HT processes between the FNR variants and the coenzyme.

Evolution of the spectral changes observed during the HT reactions of different $FNR_{ox/hq}$ mutants (25 μM) with $NADP^+$/H (100 μM) in 50 mM Tris/HCl, pH 8.0 at 6ºC. Reduction of **(A)** WT, **(B)** Y104F, **(C)** E103Y/Y104F/S109F/G110P and **(D)** E267A/E268M FNR_{ox} with NADPH and oxidation of **(E)** WT, **(F)** Y104F, **(G)** E103Y/Y104F/S109F/G110P and **(H)** E267A/E268M FNR_{hq} with $NADP^+$. In all cases spectra were recorded at 0.00128 s, 0.00384 s, 0.0064 s, 0.0192 s and 0.2547 s; the thick line is the spectrum of the oxidized/reduced protein before reacting and the inset shows the time evolution of the absorption at 458 nm.

Figure 5. Crystal structure of E103Y/Y104F/S109F/G110P FNR. (A) Comparison of the three-dimensional structures of WT (blue, FAD in green) and E103Y/Y104F/S109F/G110P (pink, FAD in yellow) *An*FNRs in the FAD environment. Detail of the H-bond between the ribose O4 atom in **(B)** WT and **(C)** E103Y/Y104F/S109F/G110P *An*FNRs. FAD and mutated side-chains are represented in CPK colored sticks.

Figure 6. Conformation of the FNR $loop_{261-269}$ along catalysis. Conformations of $loop_{261-269}$ and some of its key residues in **(A)** WT *An*FNR (PDB 1QUE, blue), and in **(B)** C-II (PDB 1GJR, grey) and **(C)** C-III (PDB 2BSA, purple) complexes with $NADP^+$ (pink pale sticks). The Thr302-Glu267 and Tyr303-Arg264 interactions are shown as dashed lines. **(D)** Superposition in the $loop_{261-269}$ region of the structure theoretically predicted for E267A/E268M FNR (pink), WT *An*FNR (PDB 1QUE, blue) and C-II FNR:$NADP^+$ complex (PDB 1GJR, grey). Side-chains for positions 263, 264, 267 and 268 are represented as CPK sticks. The E267A/E268M FNR theoretical model was produced using the Geno3D server [62] and *An*FNR WT (PDB 1QUE) as template.

Table 1. Steady-state kinetic parameters of the different FNR_{ox} variants for the interaction with $NADP^+$ and for the diaphorase activity. Measurements were carried out in 50 mM Tris/HCl, pH 8.0 at 25ºC.

FNR variant	Interaction Parameters		Diaphorase Steady-State Kinetic Parameters								
			DCPIP						$Fe(CN)_6^{3-}$		
	$NADP^+$		NADPH			NADH			NADPH		
	K_d^{NADP+} (μM)	$\Delta\varepsilon_{(482-390)}$ ($mM^{-1}cm^{-1}$)	K_m (μM)	k_{cat} (s^{-1})	k_{cat}/K_m ($\mu M^{-1}s^{-1}$)	K_m (μM)	k_{cat} (s^{-1})	k_{cat}/K_m ($\mu M^{-1}s^{-1}$)	K_m (μM)	k_{cat} (s^{-1})	k_{cat}/K_m ($\mu M^{-1}s^{-1}$)
WT [a]	4.0	1.15	6.0	81.5	13.6	800	0.16	2.0×10^{-4}	11	370	34
Y104F	2.7	1.34 [b]	6.4	84.2	13.2	665	0.35	5.3×10^{-4}	16	265	16.6
E103Y/Y104F/S109F/G110P	2.8	1.35 [c]	4.7	67.3	14.3	651	0.27	4.1×10^{-4}	14	257	18.4
E267A/E268M	1.2	1.15 [d]	2.7	67.6	25.0	518	14	2.7×10^{-2}	22	309	14

[a] data from [10]
[b] using $\Delta\varepsilon_{(484-395)}$
[c] using $\Delta\varepsilon_{(481-394)}$
[d] using $\Delta\varepsilon_{(485-396)}$

Table 2. Steady-state kinetic parameters of the different FNR_{ox} variants in the NADPH-dependent cytochrome *c* reductase activity. Measurements in 50 mM Tris/HCl, pH 8.0 at 25ºC.

FNR variant	K_m^{Fd} (μM)	k_{cat} (s^{-1})	k_{cat}/K_m ($\mu M^{-1}s^{-1}$)
WT [a]	1.0	176	176
Y104F	5.7	22.2	4
E103Y/Y104F/S109F/G110P	6.1	166.7	27
E267A/E268M	2.1	66.7	31.7

[a] data from [10]

Table 3. Parameters for the laser-flash induced reduction of the different FNR variants by dRfH• and *An*Fd_{rd}.

FNR variant	Reduction by dRfH•[a]	Reduction by *An*Fd_{rd}[b]			
	k_2 ($M^{-1}s^{-1}$)	k_1 ($\mu M^{-1}s^{-1}$)	k_{-1} (s^{-1})	k_{et} (s^{-1})	K_d (μM)
WT	2.3×10^8	6.8×10^4	22.4×10^4	7.8×10^3	3.2
E103Y/Y104F/S109F/G110P	3.8×10^8	2.5×10^4	33.4×10^4	6.4×10^3	13.3

[a] In 4mM phosphate, pH 7.0 (I = 20mM)
[b] In 4mM phosphate, pH 7.0, and 100 mM NaCl (I = 120 mM)

Table 4. Transient-kinetics parameters for the HT and HT-1 processes between the different $FNR_{hq/ox}$ and $NADP^+$/H. Measured in 50 mM Tris/HCl, pH 8.0 at 6ºC.

FNR variant	FNR_{ox} and NADPH		FNR_{hq} and $NADP^+$	
	K_d^{NADPH} (μM^{-1})	k_{HT1} (s^{-1})	K_d^{NADP+} (μM^{-1})	k_{HT-1} (s^{-1})
WT	--	270	--	290
Y104F	--	277	--	281
E103Y/Y104F/S109F/G110P	--	247	--	287
E267A/E268M	18.6	290	--	133

References

[1] A.K. Arakaki, E.A. Ceccarelli, N. Carrillo, Plant-type ferredoxin-NADP$^+$ reductases: a basal structural framework and a multiplicity of functions, FASEB J 11 (1997) 133-140.

[2] E.A. Ceccarelli, A.K. Arakaki, N. Cortez, N. Carrillo, Functional plasticity and catalytic efficiency in plant and bacterial ferredoxin-NADP(H) reductases, Biochim Biophys Acta 1698 (2004) 155-165.

[3] M. Medina, Structural and mechanistic aspects of flavoproteins: photosynthetic electron transfer from photosystem I to NADP$^+$, FEBS J 276 (2009) 3942-3958.

[4] A. Aliverti, V. Pandini, A. Pennati, M. de Rosa, G. Zanetti, Structural and functional diversity of ferredoxin-NADP$^+$ reductases, Arch Biochem Biophys 474 (2008) 283-291.

[5] P.A. Karplus, C.M. Bruns, Structure-function relations for ferredoxin reductase, J Bioenerg Biomembr 26 (1994) 89-99.

[6] N. Carrillo, E.A. Ceccarelli, Open questions in ferredoxin-NADP$^+$ reductase catalytic mechanism, Eur J Biochem 270 (2003) 1900-1915.

[7] I. Lans, M. Medina, E. Rosta, G. Hummer, M. García-Viloca, J.M. Lluch, A. González-Lafont, Theoretical study of the mechanism of the hydride transfer between ferredoxin-NADP$^+$ reductase and NADP$^+$: The Role of Tyr303, J Am Chem Soc 134 (2012) 20544-20553.

[8] A. Sánchez-Azqueta, M.A. Musumeci, M. Martínez-Júlvez, E.A. Ceccarelli, M. Medina, Structural backgrounds for the formation of a catalytically competent complex with NADP(H) during hydride transfer in ferredoxin-NADP$^+$ reductases, Biochim Biophys Acta 1817 (2012) 1063-1071.

[9] A. Sánchez-Azqueta, B. Herguedas, R. Hurtado-Guerrero, M. Hervás, J.A. Navarro, M. Martínez-Júlvez, M. Medina, A hydrogen bond network in the active site of *Anabaena* Ferredoxin-NADP$^+$ reductase modulates its catalytic efficiency, Biochim Biophys Acta (2013).

[10] A. Sanchez-Azqueta, B. Herguedas, R. Hurtado-Guerrero, M. Hervas, J.A. Navarro, M. Martinez-Julvez, M. Medina, A hydrogen bond network in the active site of Anabaena ferredoxin-NADP$^+$ reductase modulates its catalytic efficiency, Biochim Biophys Acta (2013).

[11] P.A. Karplus, M.J. Daniels, J.R. Herriott, Atomic structure of ferredoxin-NADP$^+$ reductase: prototype for a structurally novel flavoenzyme family, Science 251 (1991) 60-66.

[12] M. Medina, C. Gómez-Moreno, Interaction of ferredoxin-NADP$^+$ reductase with its substrates: optimal interaction for efficient electron transfer, Photosynth Res 79 (2004) 113-131.

[13] J.K. Hurley, R. Morales, M. Martínez-Júlvez, T.B. Brodie, M. Medina, C. Gómez-Moreno, G. Tollin, Structure-function relationships in *Anabaena* ferredoxin/ferredoxin-NADP$^+$ reductase electron transfer: insights from site-directed mutagenesis, transient absorption spectroscopy and X-ray crystallography, Biochim Biophys Acta 1554 (2002) 5-21.

[14] L. Serre, F.M. Vellieux, M. Medina, C. Gómez-Moreno, J.C. Fontecilla-Camps, M. Frey, X-ray structure of the ferredoxin:NADP$^+$ reductase from the cyanobacterium *Anabaena* PCC 7119 at 1.8 Å resolution, and crystallographic studies of NADP$^+$ binding at 2.25 Å resolution, J Mol Biol 263 (1996) 20-39.

[15] Z. Deng, A. Aliverti, G. Zanetti, A.K. Arakaki, J. Ottado, E.G. Orellano, N.B. Calcaterra, E.A. Ceccarelli, N. Carrillo, P.A. Karplus, A productive NADP$^+$ binding mode of ferredoxin-NADP$^+$ reductase revealed by protein engineering and crystallographic studies, Nat Struct Biol 6 (1999) 847-853.

[16] C.M. Bruns, P.A. Karplus, Refined crystal structure of spinach ferredoxin reductase at 1.7 Å resolution: oxidized, reduced and 2'-phospho-5'-AMP bound states, J Mol Biol 247 (1995) 125-145.

[17] I. Nogués, I. Pérez-Dorado, S. Frago, C. Bittel, S.G. Mayhew, C. Gómez-Moreno, J.A. Hermoso, M. Medina, N. Cortez, N. Carrillo, The ferredoxin-NADP(H) reductase from *Rhodobacter capsulatus*: molecular structure and catalytic mechanism, Biochemistry 44 (2005) 11730-11740.

[18] M. Ingelman, S. Ramaswamy, V. Niviere, M. Fontecave, H. Eklund, Crystal structure of NAD(P)H:flavin oxidoreductase from Escherichia coli, Biochemistry 38 (1999) 7040-7049.

[19] G. Lu, Y. Lindqvist, G. Schneider, U. Dwivedi, W. Campbell, Structural studies on corn nitrate reductase: refined structure of the cytochrome *b* reductase fragment at 2.5 Å, its ADP complex and an active-site mutant and modeling of the cytochrome *b* domain, J Mol Biol 248 (1995) 931-948.

[20] M.C. Bewley, C.C. Marohnic, M.J. Barber, The structure and biochemistry of NADH-dependent cytochrome b_5 reductase are now consistent, Biochemistry 40 (2001) 13574-13582.

[21] J. Tejero, J.R. Peregrina, M. Martínez-Júlvez, A. Gutiérrez, C. Gómez-Moreno, N.S. Scrutton, M. Medina, Catalytic mechanism of hydride transfer between $NADP^+$/H and ferredoxin-$NADP^+$ reductase from *Anabaena* PCC 7119, Arch. Biochem. Biophys. 459 (2007) 79-90.

[22] J.R. Peregrina, A. Sánchez-Azqueta, B. Herguedas, M. Martínez-Júlvez, M. Medina, Role of specific residues in coenzyme binding, charge-transfer complex formation, and catalysis in *Anabaena* ferredoxin-$NADP^+$ reductase, Biochim Biophys Acta 1797 (2010) 1638-1646.

[23] M. Medina, M. Martínez-Júlvez, J.K. Hurley, G. Tollin, C. Gómez-Moreno, Involvement of glutamic acid 301 in the catalytic mechanism of ferredoxin-$NADP^+$ reductase from *Anabaena* PCC 7119, Biochemistry 37 (1998) 2715-2728.

[24] I. Nogués, J. Tejero, J.K. Hurley, D. Paladini, S. Frago, G. Tollin, S.G. Mayhew, C. Gómez-Moreno, E.A. Ceccarelli, N. Carrillo, M. Medina, Role of the C-terminal tyrosine of ferredoxin-nicotinamide adenine dinucleotide phosphate reductase in the electron transfer processes with its protein partners ferredoxin and flavodoxin, Biochemistry 43 (2004) 6127-6137.

[25] M. Martínez-Júlvez, J. Hermoso, J.K. Hurley, T. Mayoral, J. Sanz-Aparicio, G. Tollin, C. Gómez-Moreno, M. Medina, Role of Arg100 and Arg264 from *Anabaena* PCC 7119 ferredoxin-$NADP^+$ reductase for optimal $NADP^+$ binding and electron transfer, Biochemistry 37 (1998a) 17680-17691.

[26] D.H. Paladini, M.A. Musumeci, N. Carrillo, E.A. Ceccarelli, Induced fit and equilibrium dynamics for high catalytic efficiency in ferredoxin-NADP(H) reductases, Biochemistry 48 (2009) 5760-5768.

[27] J.A. Hermoso, T. Mayoral, M. Faro, C. Gomez-Moreno, J. Sanz-Aparicio, M. Medina, Mechanism of coenzyme recognition and binding revealed by crystal structure analysis of ferredoxin-$NADP^+$ reductase complexed with $NADP^+$, J Mol Biol 319 (2002) 1133-1142.

[28] C.C. Correll, C.J. Batie, D.P. Ballou, M.L. Ludwig, Phthalate dioxygenase reductase: a modular structure for electron transfer from pyridine nucleotides to [2Fe-2S], Science 258 (1992) 1604-1610.

[29] H. Nishida, K. Inaka, M. Yamanaka, S. Kaida, K. Kobayashi, K. Miki, Crystal structure of NADH-cytochrome b_5 reductase from pig liver at 2.4 Å resolution, Biochemistry 34 (1995) 2763-2767.

[30] C.C. Marohnic, M.C. Bewley, M.J. Barber, Engineering and characterization of a NADPH-utilizing cytochrome b_5 reductase, Biochemistry 42 (2003) 11170-11182.

[31] M. Medina, A. Luquita, J. Tejero, J. Hermoso, T. Mayoral, J. Sanz-Aparicio, K. Grever, C. Gómez-Moreno, Probing the determinants of coenzyme specificity in ferredoxin-$NADP^+$ reductase by site-directed mutagenesis, J Biol Chem 276 (2001) 11902-11912.

[32] J. Tejero, M. Martínez-Júlvez, T. Mayoral, A. Luquita, J. Sanz-Aparicio, J.A. Hermoso, J.K. Hurley, G. Tollin, C. Gómez-Moreno, M. Medina, Involvement of the pyrophosphate and the 2'-phosphate binding regions of ferredoxin-$NADP^+$ reductase in coenzyme specificity, J. Biol. Chem. 278 (2003) 49203-49214.

[33] J.R. Peregrina, B. Herguedas, J.A. Hermoso, M. Martínez-Júlvez, M. Medina, Protein motifs involved in coenzyme interaction and enzymatic efficiency in *Anabaena* ferredoxin-$NADP^+$ reductase, Biochemistry 48 (2009) 3109-3119.

[34] A. Aliverti, T. Lubberstedt, G. Zanetti, R.G. Herrmann, B. Curti, Probing the role of lysine 116 and lysine 244 in the spinach ferredoxin-$NADP^+$ reductase by site-directed mutagenesis, J Biol Chem 266 (1991) 17760-17763.

[35] S. Baroni, V. Pandini, M.A. Vanoni, A. Aliverti, A single tyrosine hydroxyl group almost entirely controls the NADPH specificity of Plasmodium falciparum ferredoxin-$NADP^+$ reductase, Biochemistry 51 (2012) 3819-3826.

[36] L. Piubelli, A. Aliverti, A.K. Arakaki, N. Carrillo, E.A. Ceccarelli, P.A. Karplus, G. Zanetti, Competition between C-terminal tyrosine and nicotinamide modulates pyridine nucleotide affinity and specificity in plant ferredoxin-$NADP^+$ reductase, J Biol Chem 275 (2000) 10472-10476.

[37] J. Tejero, I. Pérez-Dorado, C. Maya, M. Martínez-Júlvez, J. Sanz-Aparicio, C. Gómez-Moreno, J.A. Hermoso, M. Medina, C-terminal tyrosine of ferredoxin-$NADP^+$ reductase in hydride transfer processes with $NAD(P)^+$/H, Biochemistry 44 (2005) 13477-13490.

[38] I. Lans, J.R. Peregrina, M. Medina, M. García-Viloca, A. González-Lafont, J.M. Lluch, Mechanism of the hydride transfer between *Anabaena* Tyr303Ser FNR_{rd}/FNR_{ox} and $NADP^+$/H. A combined pre-steady-state kinetic/ensemble-averaged transition-state theory with multidimensional tunneling study, J Phys Chem B 114 (2010) 3368-3379.

[39] J.R. Peregrina, I. Lans, M. Medina, The transient catalytically competent coenzyme allocation into the active site of *Anabaena* ferredoxin-$NADP^+$ reductase, Eur Biophys J (2012).

[40] P. Macheroux, UV-visible spectroscopy as a tool to study flavoproteins, Methods Mol Biol 131 (1999) 1-7.

[41] V. Rodríguez-Roldán, J.M. García-Heredia, J.A. Navarro, M. Hervás, B. De la Cerda, F.P. Molina-Heredia, M.A. De la Rosa, A comparative kinetic analysis of the reactivity of plant, horse, and human respiratory cytochrome *c* towards cytochrome *c* oxidase, Biochem Biophys Res Commun 346 (2006) 1108-1113.

[42] T.E. Meyer, Z.G. Zhao, M.A. Cusanovich, G. Tollin, Transient kinetics of electron transfer from a variety of *c*-type cytochromes to plastocyanin, Biochemistry 32 (1993) 4552-4559.

[43] S. Daff, An appraisal of multiple NADPH binding-site models proposed for cytochrome P450 reductase, NO synthase, and related diflavin reductase systems, Biochemistry 43 (2004) 3929-3932.

[44] W. Kabsch, Automatic processing of rotation diffraction data from crystals of initially unkown symmetry and cell constants, J Appl Cryst 26 (1993) 795-800.

[45] M.D. Winn, C.C. Ballard, K.D. Cowtan, E.J. Dodson, P. Emsley, P.R. Evans, R.M. Keegan, E.B. Krissinel, A.G. Leslie, A. McCoy, S.J. McNicholas, G.N. Murshudov, N.S. Pannu, E.A. Potterton, H.R. Powell, R.J. Read, A. Vagin, K.S. Wilson, Overview of the CCP4 suite and current developments, Acta Crystallogr D Biol Crystallogr 67 (2011) 235-242.

[46] A. Vagin, A. Teplyakov, MOLREP: an automated program for molecular replacement J. Appl. Cryst. 30 (1997) 1022-1025.

[47] G.N. Murshudov, A.A. Vagin, E.J. Dodson, Refinement of macromolecular structures by the maximum-likelihood method, Acta Crystallogr D Biol Crystallogr 53 (1997) 240-255.

[48] P. Emsley, B. Lohkamp, W.G. Scott, K. Cowtan, Features and development of Coot, Acta Crystallogr D Biol Crystallogr 66 (2010) 486-501.

[49] R.A. Laskowski, M.W. MacArthur, D.S. Moss, J.M. Thornton, PROCHECK: a program to check the stereochemical quality of protein structures, J. Appl. Cryst. 26 (1993) 283-291.

[50] I.W. Davis, A. Leaver-Fay, V.B. Chen, J.N. Block, G.J. Kapral, X. Wang, L.W. Murray, W.B. Arendall, 3rd, J. Snoeyink, J.S. Richardson, D.C. Richardson, MolProbity: all-atom contacts and structure validation for proteins and nucleic acids, Nucleic Acids Res 35 (2007) W375-383.

[51] J.K. Hurley, J.L. Schmeits, C. Genzor, C. Gómez-Moreno, G. Tollin, Charge reversal mutations in a conserved acidic patch in *Anabaena* ferredoxin can attenuate or enhance electron transfer to ferredoxin:$NADP^+$ reductase by altering protein/protein orientation within the intermediate complex, Arch Biochem Biophys 333 (1996) 243-250.

[52] S. Frago, I. Lans, J.A. Navarro, M. Hervás, D.E. Edmondson, M.A. De la Rosa, C. Gómez-Moreno, S.G. Mayhew, M. Medina, Dual role of FMN in flavodoxin function: electron transfer cofactor and modulation of the protein-protein interaction surface, Biochim Biophys Acta 1797 (2010) 262-271.

[53] M.A. Musumeci, H. Botti, A. Buschiazzo, E.A. Ceccarelli, Swapping FAD binding motifs between plastidic and bacterial ferredoxin-NADP(H) reductases, Biochemistry 50 (2011) 2111-2122.

[54] R. Morales, M.H. Charon, G. Kachalova, L. Serre, M. Medina, C. Gómez-Moreno, M. Frey, A redox-dependent interaction between two electron-transfer partners involved in photosynthesis, EMBO Rep 1 (2000) 271-276.

[55] J.K. Hurley, A.M. Weber-Main, M.T. Stankovich, M.M. Benning, J.B. Thoden, J.L. Vanhooke, H.M. Holden, Y.K. Chae, B. Xia, H. Cheng, J.L. Markley, M. Martínez-Júlvez, C. Gómez-Moreno, J.L. Schmeits, G. Tollin, Structure-function relationships in *Anabaena* ferredoxin: correlations between X-ray crystal structures, reduction potentials, and rate constants of electron transfer to ferredoxin:$NADP^+$ reductase for site-specific ferredoxin mutants, Biochemistry 36 (1997) 11100-11117.

[56] V.I. Dumit, T. Essigke, N. Cortez, G.M. Ullmann, Mechanistic insights into ferredoxin-NADP(H) reductase catalysis involving the conserved glutamate in the active site, J Mol Biol 397 (2010) 814-825.

[57] C.J. Batie, H. Kamin, Electron transfer by ferredoxin:$NADP^+$ reductase. Rapid-reaction evidence for participation of a ternary complex, J Biol Chem 259 (1984a) 11976-11985.

[58] C.J. Batie, H. Kamin, Ferredoxin:NADP+ oxidoreductase. Equilibria in binary and ternary complexes with NADP+ and ferredoxin, J Biol Chem 259 (1984b) 8832-8839.

[59] J. Sancho, C. Gómez-Moreno, Interaction of ferredoxin-$NADP^+$ reductase from *Anabaena* with its substrates, Arch Biochem Biophys 288 (1991) 231-238.

[60] A. Aliverti, R. Faber, C.M. Finnerty, C. Ferioli, V. Pandini, A. Negri, P.A. Karplus, G. Zanetti, Biochemical and crystallographic characterization of ferredoxin-$NADP^+$ reductase from nonphotosynthetic tissues, Biochemistry 40 (2001) 14501-14508.

[61] Y. Onda, T. Matsumura, Y. Kimata-Ariga, H. Sakakibara, T. Sugiyama, T. Hase, Differential interaction of maize root ferredoxin:$NADP^+$ oxidoreductase with photosynthetic and non-photosynthetic ferredoxin isoproteins, Plant Physiol 123 (2000) 1037-1045.

[62] C. Combet, M. Jambon, G. Deléage, C. Geourjon, Geno3D: automatic comparative molecular modelling of protein, Bioinformatics/computer Applications in The Biosciences 18 (2002) 213-214.

External loops at the ferredoxin-NADP+ reductase protein-partner binding cavity contribute to substrates allocation

Ana Sánchez-Azqueta[1], Marta Martínez-Júlvez[1], Manuel Hervás[2], José A. Navarro[2], and Milagros Medina[1]

[1]*Departamento de Bioquímica y Biología Molecular y Celular, Facultad de Ciencias, and Institute of Biocomputation and Physics of Complex Systems (BIFI)-Joint Unit BIFI-IQFR (CSIC), Universidad de Zaragoza, Zaragoza, Spain.*
[2]*Instituto de Bioquímica Vegetal y Fotosíntesis, cicCartuja, Universidad de Sevilla & CSIC, Sevilla, Spain.*

Running Title: FNR external loops contribute to substrates allocation

Keywords: Ferredoxin-NADP$^+$ reductase, electron and hydride transfer, isoalloxazine:nicotinamide interaction, catalytically competent interaction, charge-transfer complex.

Correspondence to: Milagros Medina. Departamento de Bioquímica y Biología Molecular y Celular. Facultad de Ciencias. Universidad de Zaragoza. E-50009 Zaragoza. Spain. Fax +34 976 762123, Phone: +34 976 762476. E-mail: mmedina@unizar.es

Abbreviations: FNR, ferredoxin-NADP$^+$ reductase; FNR_{ox}, FNR in the fully oxidized state; FNR_{sq}, FNR in the partially reduced state; FNR_{hq}, FNR in the anionic hydroquinone (fully reduced) state; ET, electron transfer; HT, hydride transfer; WT, wild-type; CTC, charge-transfer complex; NMN, nicotinamide nucleotide moiety of NADP$^+$/H; 2'-P-AMP, 2'-P-AMP moiety of NADP$^+$/H; PPi, pyrophosphate; k_{HT}, k_{HT-1}, hydride transfer first-order rate constants for the forward and reverse reactions, respectively; k_{et}, electron transfer rate constant.

Acknowledgements: This work has been supported by MINECO, Spain (Grant BIO2010-14983 to M.M) and the Andalusian Government-FEDER (PAIDI BIO-022 to J.A.N.). A. S-A holds a FPU fellowship from the Spanish Ministry of Education.

Summary

Ferredoxin-$NADP^+$ reductase (FNR) is the structural prototype of a family of FAD-containing reductases that catalyze electron transfer between low potential proteins and $NAD(P)^+/H$, and that display a two-domain arrangement with an open cavity at their interface. The inner part of this cavity accommodates the reacting atoms during catalysis. Loops at its edge are highly conserved among plastidic FNRs, suggesting they might contribute to both flavin stabilization and competent disposition of substrates. Here we pay attention to two of these loops in *Anabaena* FNR. The first is a sheet-loop-sheet motif, $loop_{102-114}$, that allocates the FAD adenosine. It was thought to determine the extended FAD conformation, and, indirectly, to modulate isoalloxazine electronic properties, partners binding, catalytic efficiency and even coenzyme specificity. The second, $loop_{261-269}$, contains key residues for the allocation of partners and coenzyme, including two glutamates, Glu267 and Glu268, proposed as candidates to facilitate the key displacement of the C-terminal tyrosine (Tyr303) from its stacking against the isoalloxazine ring during the catalytic cycle. Our data indicate that the main function of $loop_{102-114}$ is to provide the inter-domain cavity with flexibility to accommodate protein partners and to guide the coenzyme to the catalytic site, while the extended conformation of FAD must be induced by other protein determinants. Glu267 and Glu268 appear to assist the conformational changes that occur in the $loop_{261-269}$ during productive coenzyme binding, but their contribution to Tyr303 displacement is minor than expected. Additionally, $loop_{261-269}$ appears a determinant to ensure reversibility in photosynthetic FNRs.

Introduction

Ferredoxin-NADP$^+$ reductases (FNR) from photosynthetic organisms catalyze the production of NADPH in plants and cyanobacteria [1-3]. Their mechanisms are well characterized and they are the structural prototype for a large family of flavin-dependent oxido-reductases that participate in several biological reactions such as nitrogen fixation, steroid metabolism, iron-sulfur cluster biogenesis and oxidative-stress response [4, 5]. Nevertheless, recent studies have indicated that additional residues to those directly implicated in the catalytic event, might also have an important contribution at the molecular level to the enzyme functionality [3, 6-10]. Members of the family share the presence of a basic module consisting on a flavin-binding domain (FAD or FMN) and a pyridine nucleotide-binding domain (NAD(P)$^+$/H) [11]. Generally, the cavity at the interface between the two domains contains the electron carrier protein partner (ferredoxin (Fd) or flavodoxin (Fld)) binding site. Affinity and stability of the FNR complexes with its partners are mainly defined by direct contacts through their binding regions, but structural views indicate that more distant protein regions might also contribute to the overall process (**Figure SM1**) [3, 12, 13].

Structural comparison of some FNR-like representatives indicates differences in the conformation of their FAD cofactors (**Figure 1A**). In plastidic-type FNRs the FAD is held in a L-shaped extended conformation, where the PPi group acts as a hinge and the adenosine moiety is bound to a flexible sheet-loop-sheet motif ($loop_{102-114}$ in *Anabaena* FNR (*An*FNR)) where particular interactions are produced among the adenosine of FAD and the Tyr104 side-chain (including π-π stacking and a H-bond between the adenosine O4 atom and the Tyr104 hydroxyl) [14-16]. In NAD-dependent proteins of the same structural family, such as nitrate reductases (NR) or cytochrome b_5 reductases (Cb5R), as well as in FNRs from proteobacteria, FAD shows different folded conformations [17-20]: for example, in rat Cb5R (*r*Cb5R) the adenosine folds back, and sandwiched between a Tyr and a Phe (**Figures 1A and 1C**). Moreover, the catalytic efficiencies of bacterial FNR homologues and of NAD-dependent reductases, as well as their midpoint reduction potentials, differ from those of plastidic FNRs, inferring some relationship between these properties and the flavin conformation.

Electron (ET) and hydride (HT) transfer steps involving $FNR_{hq/ox}$ and $NADP^+/H$ or $Fd_{ox/rd}/Fld_{sq/hq}$ are in general very fast processes, in which the enzyme specifically recognizes its partners and brings the reacting atoms into an optimal geometry [3, 12, 21-25]. During HT between $FNR_{hq/ox}$ and $NADP^+/H$, the specific recognition of the phosphorylated pyridine nucleotide is guaranteed by the presence of a bipartite binding site in the enzyme that maintains inaccessible the binding cavity for the reactive nicotinamide nucleotide portion of $NADP^+/H$ (NMN) until accommodating its 2'P-AMP moiety [26, 27]. On the contrary, in NAD-dependent members of the family, the NAD-binding region consists of a preformed cavity able to accommodate the whole nucleotide without any protein re-arrangement [19, 28-30]. Replacements in the 2'-P-AMP and PPi binding regions of several FNRs have only provided minor improvements in modulating coenzyme specificity, with the only exception of the FNR from *Plasmodium falciparum* [31-35]. However, improvements in affinity for NAD^+/H were reported when remodeling the $NADP^+/H$ binding cavity to create a preformed site, but these complexes were unproductive since the NMN moiety did not reach the active site [33]. This last step of the competent placement of the NMN moiety against the isoalloxazine relies on the displacement of the C-terminal tyrosine side-chain (Tyr303 in *An*FNR). The exact forces and mechanism driving that movement still remain unknown [7, 36-38], but crystallographic data and molecular dynamic (MD) simulations pointed to a possible regulatory role played by Arg264. Its guanidinium has been detected adopting two main conformations: one interacting with the carboxylates of Glu267 and Glu268, and the other one connecting the Tyr303 terminal carboxylate (**Figure 1B** and see **Figure 4** from [39]) [14, 22, 39].

In the present work, we gain further information about the particular roles of the above mentioned regions. Guided by sequence and structure alignments, we produced and characterized a single mutant, Y104F, and a multiple mutant, E103Y/Y104F/S109F/G110P, in $loop_{102-114}$ of *An*FNR with the aim to mimic an environment that would induce a folded FAD conformation. On the other hand, the E267A/E268M *An*FNR double mutant was conceived to prevent interactions of these residues with Arg264 during the catalytic event. The binding and catalytic properties of the three *An*FNR variants, as well as their abilities for ET and HT, respectively, with Fd and $NAD(P)^+/H$, are here reported, giving further clues about their roles in substrate recognition and NMN competent entrance into the active site.

Materials and methods

Biological material

The pET28a:*An*FNR plasmids containing the Y104F, E103Y/Y104F/S109F/G110P and E267A/E268M mutations were obtained from the company Mutagenex® and used to produce the corresponding proteins from *E. coli* cultures, which were purified as previously reported [32]. *Anabaena* Fd (*An*Fd) was produced as previously described [24]. Protein samples were dialyzed in 50 mM Tris/HCl, pH 8.0 and concentrated using Amicon Ultra-15® centrifugal filters with a 10000 Dalton or a 5000 Dalton pore size for FNR or Fd, respectively. Protein preparations were made anaerobic by successive cycles of air evacuation and flushing with O_2-free Ar in 50 mM Tris/HCl, pH 8.0. FNR_{hq} variants were obtained by anaerobic photoreduction of the samples in the presence of 2 μM 5-deazariboflavin (dRf) and 3 mM EDTA in 50 mM Tris/HCl, pH 8.0 by irradiation from a 250 W light source [23].

Spectrocopic assays

Uv-Vis spectra were recorded in a Cary-100 spectrophotometer. The molar absorption coefficient for each FNR variant was spectrophotometrically determined by thermal denaturation of the protein for 10 min at 90ºC, followed by centrifugation and separation of the precipitated apoprotein, and spectroscopic quantification of the FAD released to the supernatant [40]. Photoreduction and potentiometric titrations were attempted in the presence of dRf/EDTA as previously reported [24]. These are long-lasting measurements where protein samples are illuminated and let under agitation at 25ºC, therefore, the low stability of the FNR mutants here studied prevented their full characterization. Interaction parameters with $NADP^+$ and NAD^+ were determined by difference absorption spectroscopy at 25ºC in 50 mM Tris/HCl, pH 8.0 as previously described [31]. Errors for the K_d and Δε values were ± 10% and ± 5%, respectively.

Steady-state kinetics measurements

The diaphorase activity of the FNR mutants was assayed in a double beam Cary-100 spectrophotometer using 2,6-dichlorophenolindophenol (DCPIP) ($\Delta\varepsilon_{620nm}$ 21 $mM^{-1}.cm^{-1}$) or $K_3Fe(CN)_6$ ($\Delta\varepsilon_{420nm}$ 1.05 $mM^{-1}.cm^{-1}$) as two- or one-electron acceptors,

respectively, and NADPH or NADH as electron donors. All measurements were carried out in 50 mM Tris/HCl, pH 8.0 at 25ºC. The final reaction mixture contained 4 nM FNR, either 0.1 mM DCPIP or 1.5 mM $K_3Fe(CN)_6$, and NADPH in the range 0-200 µM, or 1 µM FNR and higher nucleotide concentrations (0-5 mM) when assayed with NADH, while the reference cuvette contained 0.06 mM DCPIP when using this acceptor. The NADPH-dependent cytochrome *c* (Cyt*c*) reductase activity was determined using recombinant *An*Fd, and horse heart Cyt*c* as final electron acceptor. Reaction mixtures contained 4 nM FNR, 200 µM NADPH, 0.75 mg/ml Cyt*c* and 0-15 µM *An*Fd. Kinetic results were analyzed using a Michaelis-Menten model, and K_m and k_{cat} values were obtained by fitting the dependence of the observed initial rates on coenzyme concentration to this equation. Estimated errors in K_m and k_{cat} were ± 10% and ± 5%, respectively, for the diaphorase measurements, and ± 20 % for the Cyt*c* activity.

Laser-flash induced kinetics

Time resolved ET reactions from *An*Fd_{rd} to WT and E103Y/Y104F/S109F/G110P FNR_{ox} were measured using laser-flash photolysis at 25ºC under anaerobic conditions in a 1 cm path-length cuvette, using EDTA as electron donor and dRf as photosensitizer, as previously described [41]. The standard reaction mixture contained, in a final volume of 1.5 mL, 4 mM sodium phosphate, pH 7.0, 1 mM EDTA and 100 µM dRf, in the presence (standard buffer) or the absence (low ionic strength (*I*) buffer) of 100 mM NaCl. Direct reduction of *An*FNR_{ox} by the laser-flash generated dRf semiquinone (dRfH•) was followed by measuring the decrease of absorbance at 458 nm. When both Fd in excess (40 µM) and FNR are present simultaneously in the solution, the subsequent ET process from the generated Fd_{rd} to FNR_{ox} can be monitored as the increase of absorbance at 600 nm due to the production of FNR_{sq} [10, 13, 23, 24]. Control experiments collected at 489-500 nm, an isosbestic point of the $FNR_{ox/sq}$ couple, allowed monitoring the oxidation of Fd_{rd}, yielding rate constants that were the same, within experimental error, as those determined from the 600 nm data. The effect of the ionic strength in the reaction was analyzed by adding aliquots of a 5 M NaCl solution to a reaction cuvette containing 40 µM *An*Fd and 30 µM *An*FNR in low *I* buffer. All experiments were performed under pseudo-first-order conditions, for which the amount of acceptor (FNR_{ox}) was maintained well in excess

over the amount of the generated Fd_{rd} (<1 μM). Each kinetic trace was the average of 8-15 measurements. All kinetic traces were fitted to monoexponential curves by using the Marquardt method to obtain the pseudo-first observed rate constants (k_{obs}). Non-linear k_{obs} dependences on FNR concentration were adjusted to a two-step mechanism [23, 42],

$$Fd_{rd} + FNR_{ox} \underset{k_{-1}}{\overset{k_1}{\rightleftharpoons}} [Fd_{rd}{:}FNR_{ox}] \overset{k_{et}}{\rightarrow} Fd_{ox} + FNR_{sq}$$

to estimate minimal values of both the forward association (k_1) and reverse dissociation (k_{-1}) rate constants, as well as the equilibrium dissociation constant ($K_d = k_{-1}/k_1$) and the ET rate constant (k_{et}). Errors in the estimated values of K_d and k_{et} were ± 20% and ± 10%, respectively.

Stopped-flow pre-steady-state kinetic measurements

Fast HT processes between the $FNR_{hq/ox}$ variants and $NADP^+$/H, as well as between E267A/E268M $FNR_{hq/ox}$ and NAD^+/H were followed by stopped-flow using an *Applied Photophysics* SX17.MV equipment with a photodiode array detector. Measurements were carried out in 50 mM Tris/HCl, pH 8.0 at 6ºC under anaerobic conditions as previously described [8, 21]. Final FNR concentrations were 25 μM, while a 25-250 μM range was used for the nucleotide. Absorption spectra (400-1000 nm) were collected every 2.5 ms and processed using the X-Scan software (*App. Photo. Ltd.*). Analysis of time dependent spectral changes was performed by global analysis and numerical integration methods using Pro-Kineticist (*App. Photo. Ltd.*). The observed conversion rate constants ($k_{A\rightarrow B}$, $k_{B\rightarrow C}$) were calculated by fitting the collected data to a single step model. In most cases, a previous reaction (A→B) had occurred within the instrumental death time, leading to charge transfer complex (CTC) formation. In those cases we correlate the measurable reaction to a B→C model, being B and C spectral species reflecting a distribution of enzyme intermediates (reactants, CTCs, products, Michaelis complexes) at a certain point along the reaction time course, and not necessarily a single distinct enzyme intermediate. Model validity was assessed by lack of systematic deviations from residual plots at different wavelengths, inspection of calculated spectra and consistence among the number of significant singular values with the fitting model. In general, no dependence profiles on the $NADP^+$/H concentration

were observed for the HT processes analyzed, probably due to the reversibility of the processes and the maximal $k_{B\rightarrow C}$ values were obtained at the 1:1. Since it was not possible to determine reduction midpoint potentials for the mutants here analyzed we were not able to globally fit the apparent rate constants as a function of coenzyme concentration to the sum of the rates for the forward (k_{HT}) and reverse (k_{HT-1}) HT at equilibrium [22, 43]. Therefore, as accepted in similar cases [8, 21], we related $k_{B\rightarrow C}$ with the maximal experimental HT rate constant, k_{HT} or k_{HT-1}, values. For the reduction of E267A/E268M FNR, $k_{A\rightarrow B}$ derived from experimental data showed a dependence profile on the NADPH concentration fitting to the equation describing binding at a single site followed by the HT process,

$$k_{A\rightarrow B} = \frac{k_{HT-1}(K_d+/NADPH)+k_{HT}[NADPH]}{[NADPH]+K_d}$$

and allowed the determination of K_d and k_{HT} values. Errors in the estimated values of K_d and k_{HT} values were ± 20% and ± 15%, respectively, while those of $k_{A\rightarrow B}$ or $k_{B\rightarrow C}$ were ± 10%.

Crystal growth, data collection and structure refinement

The E103Y/Y104F/S109F/G110P variant of *An*FNR was crystallized under same conditions as those reported for WT FNR [27]. X-ray data set was collected in the ID23-1 line at ESRF (Grenoble, France) and processed with XDS [44] and SCALA from CCP4 [45]. The first model was obtained by MOLREP [46] from CCP4, using the WT FNR structure (1QUE) as template. Refinement of the structure was performed with Refmac5 [47] from CCP4, alternating with manual model building with COOT [48]. PROCHECK [49] and MOLPROBITY [50] programs were used to assess final structure. A single crystal of E103Y/Y104F/S109F/G110P FNR diffracted up to 1.70 Å and belonged to the $P6_5$ hexagonal space group. Its V_m was 2.95 $Å^3$/Da with one FNR molecule in the asymmetric unit and 58.4 % solvent content. The model comprised residues 9-303, one FAD molecule, one SO_4^{2-} ion, one glycerol molecule and water molecules. Data for collection and refinement processes can be found in Table SP1. The coordinates and structure factors for this FNR variant have been deposited with PDB ID: 4C43.

Results

Spectral properties of the FNR_{ox} variants and interaction with the coenzyme

The level of expression in *E. coli* of all the FNR mutants was similar to that of WT, and purification yielded well-folded and FAD assembled FNRs. The mutants showed similar spectral properties to WT *An*FNR_{ox}, with absorbance maxima of the flavin band-I at 458 nm and extinction coefficients at this wavelength not varying significantly, indicating no major structural perturbations in the close environment of the FAD isoalloxazine ring. However, Y104F FNR suffered some loss of the FAD cofactor when dialyzed, and E267A/E268M FNR was not soluble at concentrations over 60 μM. Moreover, stepwise photoreduction of Y104F, E103Y/Y104F/S109F/G110P and E267A/E268M FNRs induced FAD dissociation and protein denaturation, preventing determination of their midpoint reduction potentials. These observations indicate that the mutations particularly affect the strength of the ApoFNR:FAD_{hq} complex, suggesting weakening of the affinity for the reduced form of the cofactor.

Difference spectra obtained upon titration of Y104F, E103Y/Y104F/S109F/G110P and E267A/E268M FNRs with $NADP^+$ were similar to those for the WT protein, with only minor displacements of the positions of minima and maxima (**Figure 2**). The hyperbolic dependence of the absorbance changes upon increasing $NADP^+$ concentrations allowed determination of K_d^{NADP+} as well as of the magnitude of the change upon complex formation, Δε (**Table 1**). K_d^{NADP+} did not vary significantly either being just slightly smaller, 1.5-fold for the Y104F and E103Y/Y104F/S109F/G110P FNRs, or up to 3.3-fold for E267A/E268M FNR. Therefore while the $loop_{102-114}$ appears to have minor effects on $NADP^+$ binding, the glutamates in positions 267 and/or 268 in the WT enzyme appear contributing to reduce the affinity for this form of the coenzyme. Titration of all FNR variants with NAD^+ did not induce any difference spectra, indicating that this coenzyme was not able to produce changes in the flavin environment. This suggests that its nicotinamide ring is not bound in the enzyme flavin environment.

Steady-state kinetic parameters of the FNR mutants

Either DCPIP or potassium ferricyanide, as final artificial two- or one- electron acceptors respectively, were used to obtain the diaphorase steady-state kinetic parameters of the FNR variants (**Table 1**). Y104F and E103Y/Y104F/S109F/G110P

FNRs displayed behaviors very similar to that of WT, though in general k_{cat} values slightly decreased. Regarding E267A/E268M FNR, k_{cat} values were also slightly lower and K_m^{NADPH} values were within 2-fold of those of the WT: increasing when using ferricyanide as electron acceptor and decreasing when using DPCIP. Therefore, the E267A/E268M FNR catalytic efficiency increased around 2-fold when using a two-electron acceptor, while decreased in a similar range when using a one-electron acceptor. Finally, the diaphorase activity of E267A/E268M FNR showed a remarkable k_{cat} increase regarding WT FNR when using NADH as electron donor. As consequence, this variant was two orders of magnitude less specific for NADPH *versus* NADH than the WT.

The introduced mutations produced more important deleterious effects in the Fd mediated NADPH dependent Cyt*c* reductase activity of FNR (**Table 2)**. Despite E103Y/Y104F/S109F/G110P FNR exhibited a similar behavior to the WT in terms of k_{cat}, this parameter resulted reduced by 8- and 2.5-fold for Y104F and E267A/E268M FNRs, respectively. Moreover, K_m^{Fd} increased for all the variants, but particularly for those at $loop_{102-114}$, suggesting that the mutations reduce the affinity of FNR for Fd, at least in an optimal orientation for ET. All together these parameters indicate that the introduced mutations, but particularly the single replacement of Tyr104 by Phe, have an important negative impact in the non-photosynthetic ET from FNR to Fd.

Transient kinetics for ET from Fd to FNR

The low stability of Y104F and E267A/E268M FNRs prevented their characterization by laser-flash spectroscopy. However, direct reduction of the E103Y/Y104F/S109F/G110P FNR isoalloxazine to its neutral semiquinone form by the laser-flash generated dRfH• could be followed by a decrease of the absorption at 458 nm following a monoexponential decay, as observed for the WT FNR [23]. k_{obs} values resulted linearly dependent on the FNR concentration and allowed obtaining second-order bimolecular rate constants (k_2) of the same order of magnitude as for the WT (**Table 3**) [23]. This observation indicated that this mutant is as efficiently reduced by dRfH• as WT.

In the presence of an excess of Fd_{ox}, the laser-generated dRfH• causes the initial fast reduction of this protein, followed by a subsequent ET step from Fd_{rd} to FNR_{ox}, that

can be monitored by an absorption increase at 600 nm due to formation of the neutral FNR_{sq} [23, 24]. Reduction of FNR_{ox} by Fd_{rd} has been here investigated in the presence of a moderately high salt concentration (I = 120 mM), conditions reported as optimal for this ET reaction [23]. Moreover, k_{obs} values presented a hyperbolic dependence on enzyme concentration that can be related with the formation of a transient FNR_{ox}:Fd_{rd} complex prior to the ET step (**Figure 3A**) [51]. The two-step model here applied to estimate K_d and k_{et} values has largely demonstrated to be useful in the characterization of ET in transient protein:protein reactions [10, 13, 41, 42, 52]. The model is based in the total amount of FNR_{ox} in the sample as it is widely accepted that, in transient protein complexes, protein association/dissociation is much faster than ET itself, and thus the ET process would be the rate limiting step rather than protein exchange. Thus, applying the formalism previously described [42], minimal values for k_{et}, k_1 and k_{-1} (and K_d) could be estimated (**Table 3**). These values suggested a 4-fold decrease in the affinity of the Fd:FNR complex induced by the introduced mutations, whereas the ET process remains basically unaffected.

The influence of I was further analyzed to investigate the effects induced by the combined E103Y/Y104F/S109F/G110P mutations on the Fd:FNR interaction. As reported for the WT, biphasic dependences of k_{obs} with increasing I were also observed for the variant (**Figure 3B**). The bell-shaped profile for the dependence of k_{obs} with I is related with the re-arrangement of the initial FNR_{ox}:Fd_{rd} encounter transient complex to achieve an optimal ET conformation, indicating the occurrence of protein-protein dynamic motions that are blocked by strong electrostatic interactions at very low I [23]. However, the k_{obs} maximum was shifted to higher I for the mutant, suggesting the occurrence of stronger electrostatic interactions in the encounter complex than in the WT system.

Transient kinetics of the hydride transfer reactions

Fast HT processes between WT *An*$FNR_{hq/ox}$ and $NADP^+$/H occur through the formation of two intermediate CTCs [21, 22]: [FNR_{ox}-NADPH] (CTC-1, characterized by an absorbance spectral band with maximum at ~ 600 nm), and [FNR_{hq}-$NADP^+$] (CTC-2, showing a broad band centered at ~ 800 nm). The HT event occurs in the transition of CTC-1 to CTC-2, or *viceversa*. Similarly to the WT, reduction of Y104F, E103Y/Y104F/S109F/G110P and E267A/E268M *An*FNR_{ox}s by NADPH showed CTC-

1 formation and protein reduction (measurable by the decrease of the flavin band-I absorbance at 458 nm) in the instrumental death time, with subsequent spectral evolution including additional reduction of the enzyme and formation of CTC-2 (**Figures 4A-4D**). This multiple wavelength spectral evolution best fitted to a single-step model that includes the HT event, and thus the observed rate constants are named $k_{B\rightarrow C}$. For the Y104F and E103Y/Y104F/S109F/G110P variants, $k_{B\rightarrow C}$ values were independent on the NADPH concentration as in the WT, being, therefore, related with limiting k_{HT} values (**Table 4**). However, a concentration dependence hyperbolic profile was observed for the E267A/E268M FNR process allowing determination of a K_d^{NADPH} value that suggested a weaker FNR:NADPH interaction than in WT (**Table 4**). Nevertheless, significant negative effects on k_{HT} were not observed in any of the mutants.

Y104F and E103Y/Y104F/S109F/G110P FNRs also behaved very similar to WT *An*FNR when assaying the reverse reaction. Thus, reduction of $NADP^+$ by these FNR_{hq} variants showed appearance of a small amount of CTC-2 concomitant with mild protein reoxidation within the instrumental dead time, followed by subsequent spectral evolution including flavin oxidation and CTC-1 formation (**Figures 4E-4G**). Kinetic parameters for these processes were also similar to those of WT (**Table 4**). On the contrary, HT from E267A/E268M FNR_{hq} to $NADP^+$ occurred with minor CTC stabilization (**Figure 4H**), particularly of CTC-2, and with a 2-fold decrease in k_{HT-1}.

HT processes for E267A/E268M FNR were also assayed with the non-phosphorylated pyridine nucleotide, NAD^+/H, to determine if the augmented steady-state catalytic efficiency observed for this variant with NADH might be a consequence of a more efficient HT reaction. Similarly to that reported for the WT, reactions between E267A/E268M FNR and NAD^+/H were extremely slow processes that did not lead to CTC stabilization (not shown) [33]. Nevertheless, comparison of rate constants for WT and E267A/E268M FNRs using a 1:5 protein:NAD^+/H ratio, led to a slight increase in the apparent HT rate contants by the introduced mutations ($k_{A\rightarrow B}^{WT}$ = 0.02 s^{-1} and $k_{A\rightarrow B}^{E267A/E268M}$ = 0.08 s^{-1} for the reduction by NADH and $k_{A\rightarrow B}^{WT}$= 0.1 s^{-1} and $k_{A\rightarrow B}^{E267A/E268M}$ = 0.8 s^{-1} for oxidation by NAD^+).

The structural environment of the mutated positions

The overall folding of E103Y/Y104F/S109F/G110P *An*FNR is pretty similar to that of WT *An*FNR (0.73 Å for 295 Cα atoms aligned). Poor electron density did not allow determining the position of residues 106 and 107. However residues flanking them, including the mutated ones, show a good density that allows describing the peptide chain in this region. Mutations on the adenosine binding loop did not lead to a remarkable change in the overall positioning of FAD that keeps extended conformation with only its adenosine moiety differing somehow in conformation regarding to the WT structure (**Figure 5**). The absence of the Tyr104 hydroxyl, in the WT FNR H-bonding the ribose O4 atom (**Figure 5B**), is compensated by an intramolecular H-bond between both adenosine O4 and N3 atoms that seems to force a twist and a slight displacement of the adenosine moiety (**Figure 5C**). On the other hand and due to the introduced mutations, the loop shows a more open conformation than in the WT structure. So, in the mutant the $loop_{102\text{-}114}$ points outwards and differs from its WT conformation with an r.m.s.d. of 4.18 Å. Another significant structural feature observed in the mutant structure concerns to the conformation of the Arg264 side-chain (**Figure 5**). As already described in other *An*FNR structures [9, 22], its guanidinium group moves, in this mutant 5 Å, towards the Tyr303 carboxylate. This observation reinforces the idea of differently populated orientations of this Arg side-chain in position during coenzyme binding and catalysis.

Discussion

The sheet-loop-sheet motif ($loop_{102\text{-}114}$ in AnFNR) binding the FAD adenosine in plastidic FNRs

Comparison of plastidic FNRs with NAD-dependent members of the family (**Figures 1A** and **1C**) drove us to the production of two variants in the FAD adenosine binding $loop_{102\text{-}114}$: Y104F and E103Y/Y104F/S109F/G110P FNRs. The Y104F mutant was intended to disrupt the H-bond between the Tyr104-OH and the FAD adenosine, while keeping the stacking interaction with the aromatic side-chain. On the other hand, the E103Y/Y104F/S109F/G110P one was expected to induce a change in the orientation of $loop_{102\text{-}114}$ towards that displayed by some NADH-dependent members of the family (**Figure 1A**). However, the crystal structure of E103Y/Y104F/S109F/G110P FNR resulted practically identical to that of the WT protein, with the FAD in an extended conformation very similar to the WT enzyme (**Figure 5**). Moreover, the inherent flexibility of $loop_{102\text{-}114}$ and of the FAD adenosine moiety in plastidic FNRs [27, 39] is

even enhanced in the mutant. This might counteract changes in the shape of the flavin binding site introduced by the mutations. Similarly, an unaltered FAD conformation has been observed in two engineered pea and *E. coli* FNRs (plastidic- and bacterial-type FNRs, respectively) upon deletion and insertion, respectively, of the plastidic characteristic adenosine binding strand-loop-strand motif [53]. Therefore, the binding and kinetic effects induced by these mutations in *An*FNR must account mainly for changes in the nature of their side-chains rather than to the expected alterations on FAD conformation. In *An*FNR, most of the protein connections with the ribose and adenine moieties of FAD are bridged by water molecules, and only one direct H-bond is established with Tyr104-OH. Disruption of this connection in the Y104F mutant appears to have an important impact in FAD affinity, particularly in its reduced state. However, the lack of stability of this variant was recovered upon introduction of the three additional mutations in E103Y/Y104F/S109F/G110P FNR, where, although the WT contact between the FAD and the loop was still missing, a new FAD intramolecular H-bond between both adenosine O4 and N3 atoms forces a twist in the adenine orientation a the displacement of this adenosine moiety (**Figure 5**).

Apart from weaker FAD binding, substitutions in the loop$_{102\text{-}114}$ did not lead to mayor changes on FNR overall folding, nor in its NAD(P)$^+$/H binding and catalytic parameters (**Tables 1** and **4**). Nevertheless, deleterious effects were particularly observed in the affinity for the protein partner, with minor effects on ET rates (k_{et} and k_{cat}) (**Tables 1, 2** and **3**). This might be related with the clear retraction observed in the position of the loop$_{102\text{-}114}$ upon introduction of the mutations regarding those in free WT FNR and in the Fd:FNR comples, which appears having a negative effect in the initial recognition event between partners (**Figure SM2**). All together these data suggest that the main function of the loop$_{102\text{-}114}$ is to provide flexibility to the inter-domain cavity to assits guiding of the coenzyme and, particularly, of the protein partners and to their binding cavities, while other structural determinants will be responsible for the FAD extended conformation.

Role of loop$_{261\text{-}269}$ in AnFNR in the competent binding of substrates

The simultaneous substitutions of Glu267 and Glu268 in *An*FNR also affected the affinity for the protein partner (**Table 1**). The crystal structure of the *An*Fd:*An*FNR complex situates Arg264 and Glu267 at the complex interface, H-bonding Fd-

Tyr25/Arg42, and Asp62, respectively (**Figure SM3**) [13, 25, 54]. E267A/E268M FNR eliminates two negative charges on the FNR surface, as well as the possibility of H-bonding at position 267, and, conceivably the displacement of the native Arg264 arrangement might be possible. Therefore, both the initial interaction governed by electrostatic attractive forces and the subsequent optimal complex surface adjustment would be affected, thus explaining the increase on K_d^{Fd} and the decrease on k_{cat} observed for the Cyt*c* reductase activity (**Table 2**), and also in agreement with previously reported deleterious effects for the D62K *An*Fd mutant [55]. Additionally, the midpoint reduction potential appears altered in the mutant, making ET to Fd less favorable. Binding and HT data for E267A/E268M FNR with the coenzyme are indicative of higher FNR_{ox}:$NADP^+$ and lower FNR_{ox}:NADPH affinities, but with final catalytic geometries optimal and non-optimal for FNR_{ox}:NADPH and FNR_{hq}:$NADP^+$, respectively (**Tables 1** and **4**). Therefore, a role must be accepted for these two residues in coenzyme accommodation during catalysis, and in ensuring the reaction is able to take place either in the photosynthetic or non-photosynthetic directions as required by the organism, a particular feature of plastidic FNRs. This is in agreement with $loop_{261-269}$ being a determinant for competent $NADP^+$/H recognition and NMN allocation [8, 32, 33]. Thus, $loop_{261-269}$ undergoes several conformational changes during the proposed three-step (WT→C-I→C-II→C-III) $NADP^+$/H binding process [27], which involve changes in the conformation of Arg264 and Glu267 side-chains and in the interactions they establish along the transitions (**Figure 6A**). In WT and C-I, the C-terminal Tyr303 carboxylate and the Thr302-OH are situated at H-bond distance of the Arg264 amide and the Glu267 carboxylate, respectively. The transition of C-I into C-II (**Figure 6A to Figure 6B**) entails displacement of $loop_{261-269}$ and rotation of the Leu263 side-chain to accommodate the PPi and NMN moieties, breaking Arg264-Tyr303 and Glu267-Thr302 H-bonds. Finally, allocation of the NMN moiety into the active site in C-III (represented by the structure of the Y303S FNR:$NADP^+$ complex) appears accompanied by partial return of $loop_{261-269}$ to its original position (**Figure 6C**). Thus, the C-ter-$loop_{261-269}$ connections must first break apart to allow Leu263 displacement, and then get restored to assist Tyr303 displacement; two steps crucial for competent coenzyme binding. The low E267A/E268M FNR stability prevented its crystallization, but we constructed its structural model. This model suggested a displacement of $loop_{261-269}$ with respect to the original template structure, and resembled that of the C-II complex (**Figure 6B**), reinforcing the proposed influence of a Glu267-Thr302 bond in positioning of $loop_{261-}$

$_{269}$ regarding Tyr303. This conformation can explain both the higher E267A/E268M FNR_{ox}:$NADP^+$ affinity and the enhanced NADH activity due to nucleotide entrance resulting less blocked by the side-chain of Leu263, thus making 2´-AMP recognition less critical for optimal coenzyme binding (**Table 1**). Displacement of Tyr303 is hence proposed as consequence of additive forces that all together compensate for the disruption of π-π stacking and H-bond interactions with Ser80 and Glu301: the nicotinamide ring pushes Tyr303 from one side while the $loop_{261-269}$ pulls from the other. Additional concerted roles played by other protein regions are not discarded. Among them, the movement of Glu301 and the loss of its H-bond connection with Tyr303-OH [56] and the assistance by Fd binding [57, 58] may be especially relevant. According to E267A/E268M FNR k_{HT} and k_{HT-1} values (**Table 4**), contribution of $loop_{261-269}$ to Tyr303 displacement appears to be more important in the photosynthetic HT reaction, while the pushing effect of the nicotinamide would dominate the backward process. MD simulations further support this hypothesis [39]. Similarly, the HT reaction from a FNR_{hq} mutant previously produced at Arg264, R264E, to $NADP^+$ resulted slightly slowed down compared to WT, while k_{HT} values remained unaltered [25]. The different effects observed depending on the HT direction might be also related to divergences in the sequences of the $loop_{261-269}$ among plant-type reductases (**Figure 1C**). Glu267 is conserved among photosynthetic FNRs and the presence of a glutamate in the following position is characteristic of some cyanobacterial enzymes, while higher plants have a Lys and a non-polar side-chain is found in the position equivalent to Thr302. The characteristic Glu-Lys pair of leaf FNRs is replaced by a Met-Pro one in FNRs from plant roots and other non-photosynthetic organisms, such as *Leptospira interrogans* FNR. This, together with observed differences in residues at positions equivalent to $loop_{261-269}$ and NMN occupancy upon $NADP^+$ binding may be related to the preferential direction of their physiologically catalyzed reactions [11, 15, 59-61]. Thus, $loop_{261-269}$ might contain the determinants for the reversibility of the HT process in photosynthetic FNRs.

In conclusion, the *An*FNR mutants here analyzed on the FAD adenosine and $NADP^+$ binding loops further confirm the complexity of the mechanisms addressing oxido-reduction partner selectivity and catalytic efficiency in these reductases, in agreement with previous unsuccessful attempts to re-design FNRs with modified binding and/or HT properties. The results here presented conclude that the flexibility of

loop$_{102\text{-}114}$ allows a competent final relative distance of the redox catalytic centers, particularly modulating Fd binding and ET. Additionally, direct interactions between the side-chain of Arg264 and those of Glu267 and Glu268 do not play a crucial role in Tyr303 displacement, though all they participate in the $NADP^+$/H binding processes by assisting the conformational changes that occur in the loop$_{261\text{-}269}$ during productive coenzyme binding as well as to the reversibility of the HT process.

Figure Legends

Figure 1. Conformation of the FAD cofactor in the FNR family. (A) Superposition of crystal structures of *An*FNR (PDB ID: 1QUE, in green) and rat Cb5R (PDB ID: 1I7P, in purple). Residues stacking the isoalloxazine and adenosine rings of FAD are shown as sticks. The inset shows a detail of the environment of the FAD adenosine moiety, stacked between Tyr112 and Phe120 in rat Cb5R and connected through H-bond and stacking interactions with Tyr104 in *An*FNR. **(B)** Conformations of Arg264, Glu267 and Glu268 in *An*FNR (PDB ID: 1QUE, in green), in a *An*FNR:$NADP^+$ complex (PDB ID: 1GJR (known as C-II), in blue) and in Y303F *An*FNR (PDB ID: 2X3U, in yellow). **(C)** Sequence alignment of different NADP- and NAD-dependent members of the FNR superfamily (ClustalW2). Positions analyzed in this work are highlighted in green, numbers on the top correspond to the *An*FNR numbering.

Figure 2. Interaction of the FNR mutants with the coenzyme. Difference absorbance spectra elicited upon titration of WT (──), E103Y/Y104F/S109F/G110P (····) and E267A/E268M (---) FNRs (~ 20 μM) with saturating concentrations of $NADP^+$ in 50 mM Tris/HCl, pH 8.0 and 25ºC.

Figure 3. Transient ET from Fd_{rd} to E103Y/Y104F/S109F/G110P FNR_{ox}. (A) Dependence on FNR_{ox} concentration of the observed rate constants (k_{obs}) for the reduction by Fd_{rd} of WT (●) and E103Y/Y104F/S109F/G110P (■) FNR at I = 120 mM. Reaction mixtures contained 40 μM Fd_{ox}. **(B)** Dependence on the square root of I of k_{obs} for the reduction of WT (●) and E103Y/Y104F/S109F/G110P (■) FNR_{ox} by Fd_{rd}. Samples contained 30 μM FNR_{ox} and 40 μM Fd_{ox}. Reactions were carried out in 4 mM phosphate, pH 7.0 and 25ºC.

Figure 4. Transient HT processes between the FNR variants and the coenzyme.

Evolution of the spectral changes observed during the HT reactions of different $FNR_{ox/hq}$ mutants (25 μM) with $NADP^+$/H (100 μM) in 50 mM Tris/HCl, pH 8.0 at 6ºC. Reduction of **(A)** WT, **(B)** Y104F, **(C)** E103Y/Y104F/S109F/G110P and **(D)** E267A/E268M FNR_{ox} with NADPH and oxidation of **(E)** WT, **(F)** Y104F, **(G)** E103Y/Y104F/S109F/G110P and **(H)** E267A/E268M FNR_{hq} with $NADP^+$. In all cases spectra were recorded at 0.00128 s, 0.00384 s, 0.0064 s, 0.0192 s and 0.2547 s; the thick line is the spectrum of the oxidized/reduced protein before reacting and the inset shows the time evolution of the absorption at 458 nm.

Figure 5. Crystal structure of E103Y/Y104F/S109F/G110P FNR. (A) Comparison of the three-dimensional structures of WT (blue, FAD in green) and E103Y/Y104F/S109F/G110P (pink, FAD in yellow) *An*FNRs in the FAD environment. Detail of the H-bond between the ribose O4 atom in **(B)** WT and **(C)** E103Y/Y104F/S109F/G110P *An*FNRs. FAD and mutated side-chains are represented in CPK colored sticks.

Figure 6. Conformation of the FNR $loop_{261-269}$ along catalysis. Conformations of $loop_{261-269}$ and some of its key residues in **(A)** WT *An*FNR (PDB 1QUE, blue), and in **(B)** C-II (PDB 1GJR, grey) and **(C)** C-III (PDB 2BSA, purple) complexes with $NADP^+$ (pink pale sticks). The Thr302-Glu267 and Tyr303-Arg264 interactions are shown as dashed lines. **(D)** Superposition in the $loop_{261-269}$ region of the structure theoretically predicted for E267A/E268M FNR (pink), WT *An*FNR (PDB 1QUE, blue) and C-II FNR:$NADP^+$ complex (PDB 1GJR, grey). Side-chains for positions 263, 264, 267 and 268 are represented as CPK sticks. The E267A/E268M FNR theoretical model was produced using the Geno3D server [62] and *An*FNR WT (PDB 1QUE) as template.

Table 1. Steady-state kinetic parameters of the different FNR_{ox} variants for the interaction with $NADP^+$ and for the diaphorase activity. Measurements were carried out in 50 mM Tris/HCl, pH 8.0 at 25ºC.

FNR variant	Interaction Parameters		Diaphorase Steady-State Kinetic Parameters								
			DCPIP						$Fe(CN)_6^{3-}$		
	$NADP^+$		NADPH			NADH			NADPH		
	K_d^{NADP+} (μM)	$\Delta\varepsilon_{(482-390)}$ ($mM^{-1}cm^{-1}$)	K_m (μM)	k_{cat} (s^{-1})	k_{cat}/K_m ($\mu M^{-1}s^{-1}$)	K_m (μM)	k_{cat} (s^{-1})	k_{cat}/K_m ($\mu M^{-1}s^{-1}$)	K_m (μM)	k_{cat} (s^{-1})	k_{cat}/K_m ($\mu M^{-1}s^{-1}$)
WT [a]	4.0	1.15	6.0	81.5	13.6	800	0.16	2.0×10^{-4}	11	370	34
Y104F	2.7	1.34 [b]	6.4	84.2	13.2	665	0.35	5.3×10^{-4}	16	265	16.6
E103Y/Y104F/S109F/G110P	2.8	1.35 [c]	4.7	67.3	14.3	651	0.27	4.1×10^{-4}	14	257	18.4
E267A/E268M	1.2	1.15 [d]	2.7	67.6	25.0	518	14	2.7×10^{-2}	22	309	14

[a] data from [10]
[b] using $\Delta\varepsilon_{(484-395)}$
[c] using $\Delta\varepsilon_{(481-394)}$
[d] using $\Delta\varepsilon_{(485-396)}$

Table 2. Steady-state kinetic parameters of the different FNR_{ox} variants in the NADPH-dependent cytochrome *c* reductase activity. Measurements in 50 mM Tris/HCl, pH 8.0 at 25ºC.

FNR variant	K_m^{Fd} (μM)	k_{cat} (s^{-1})	k_{cat}/K_m ($\mu M^{-1}s^{-1}$)
WT [a]	1.0	176	176
Y104F	5.7	22.2	4
E103Y/Y104F/S109F/G110P	6.1	166.7	27
E267A/E268M	2.1	66.7	31.7

[a] data from [10]

Table 3. Parameters for the laser-flash induced reduction of the different FNR variants by dRfH• and *An*Fd_{rd}.

FNR variant	Reduction by dRfH•[a]	Reduction by *An*Fd_{rd}[b]			
	k_2 ($M^{-1}s^{-1}$)	k_1 ($\mu M^{-1}s^{-1}$)	k_{-1} (s^{-1})	k_{et} (s^{-1})	K_d (μM)
WT	2.3×10^8	6.8×10^4	22.4×10^4	7.8×10^3	3.2
E103Y/Y104F/S109F/G110P	3.8×10^8	2.5×10^4	33.4×10^4	6.4×10^3	13.3

[a] In 4mM phosphate, pH 7.0 (I = 20mM)
[b] In 4mM phosphate, pH 7.0, and 100 mM NaCl (I = 120 mM)

Table 4. Transient-kinetics parameters for the HT and HT-1 processes between the different $FNR_{hq/ox}$ and $NADP^+$/H. Measured in 50 mM Tris/HCl, pH 8.0 at 6ºC.

FNR variant	FNR_{ox} and NADPH		FNR_{hq} and $NADP^+$	
	K_d^{NADPH} (μM^{-1})	k_{HT1} (s^{-1})	K_d^{NADP+} (μM^{-1})	k_{HT-1} (s^{-1})
WT	--	270	--	290
Y104F	--	277	--	281
E103Y/Y104F/S109F/G110P	--	247	--	287
E267A/E268M	18.6	290	--	133

References

[1] A.K. Arakaki, E.A. Ceccarelli, N. Carrillo, Plant-type ferredoxin-NADP$^+$ reductases: a basal structural framework and a multiplicity of functions, FASEB J 11 (1997) 133-140.

[2] E.A. Ceccarelli, A.K. Arakaki, N. Cortez, N. Carrillo, Functional plasticity and catalytic efficiency in plant and bacterial ferredoxin-NADP(H) reductases, Biochim Biophys Acta 1698 (2004) 155-165.

[3] M. Medina, Structural and mechanistic aspects of flavoproteins: photosynthetic electron transfer from photosystem I to NADP$^+$, FEBS J 276 (2009) 3942-3958.

[4] A. Aliverti, V. Pandini, A. Pennati, M. de Rosa, G. Zanetti, Structural and functional diversity of ferredoxin-NADP$^+$ reductases, Arch Biochem Biophys 474 (2008) 283-291.

[5] P.A. Karplus, C.M. Bruns, Structure-function relations for ferredoxin reductase, J Bioenerg Biomembr 26 (1994) 89-99.

[6] N. Carrillo, E.A. Ceccarelli, Open questions in ferredoxin-NADP$^+$ reductase catalytic mechanism, Eur J Biochem 270 (2003) 1900-1915.

[7] I. Lans, M. Medina, E. Rosta, G. Hummer, M. García-Viloca, J.M. Lluch, A. González-Lafont, Theoretical study of the mechanism of the hydride transfer between ferredoxin-NADP$^+$ reductase and NADP$^+$: The Role of Tyr303, J Am Chem Soc 134 (2012) 20544-20553.

[8] A. Sánchez-Azqueta, M.A. Musumeci, M. Martínez-Júlvez, E.A. Ceccarelli, M. Medina, Structural backgrounds for the formation of a catalytically competent complex with NADP(H) during hydride transfer in ferredoxin-NADP$^+$ reductases, Biochim Biophys Acta 1817 (2012) 1063-1071.

[9] A. Sánchez-Azqueta, B. Herguedas, R. Hurtado-Guerrero, M. Hervás, J.A. Navarro, M. Martínez-Júlvez, M. Medina, A hydrogen bond network in the active site of *Anabaena* Ferredoxin-NADP$^+$ reductase modulates its catalytic efficiency, Biochim Biophys Acta (2013).

[10] A. Sanchez-Azqueta, B. Herguedas, R. Hurtado-Guerrero, M. Hervas, J.A. Navarro, M. Martinez-Julvez, M. Medina, A hydrogen bond network in the active site of Anabaena ferredoxin-NADP$^+$ reductase modulates its catalytic efficiency, Biochim Biophys Acta (2013).

[11] P.A. Karplus, M.J. Daniels, J.R. Herriott, Atomic structure of ferredoxin-NADP$^+$ reductase: prototype for a structurally novel flavoenzyme family, Science 251 (1991) 60-66.

[12] M. Medina, C. Gómez-Moreno, Interaction of ferredoxin-NADP$^+$ reductase with its substrates: optimal interaction for efficient electron transfer, Photosynth Res 79 (2004) 113-131.

[13] J.K. Hurley, R. Morales, M. Martínez-Júlvez, T.B. Brodie, M. Medina, C. Gómez-Moreno, G. Tollin, Structure-function relationships in *Anabaena* ferredoxin/ferredoxin-NADP$^+$ reductase electron transfer: insights from site-directed mutagenesis, transient absorption spectroscopy and X-ray crystallography, Biochim Biophys Acta 1554 (2002) 5-21.

[14] L. Serre, F.M. Vellieux, M. Medina, C. Gómez-Moreno, J.C. Fontecilla-Camps, M. Frey, X-ray structure of the ferredoxin:NADP$^+$ reductase from the cyanobacterium *Anabaena* PCC 7119 at 1.8 Å resolution, and crystallographic studies of NADP$^+$ binding at 2.25 Å resolution, J Mol Biol 263 (1996) 20-39.

[15] Z. Deng, A. Aliverti, G. Zanetti, A.K. Arakaki, J. Ottado, E.G. Orellano, N.B. Calcaterra, E.A. Ceccarelli, N. Carrillo, P.A. Karplus, A productive NADP$^+$ binding mode of ferredoxin-NADP$^+$ reductase revealed by protein engineering and crystallographic studies, Nat Struct Biol 6 (1999) 847-853.

[16] C.M. Bruns, P.A. Karplus, Refined crystal structure of spinach ferredoxin reductase at 1.7 Å resolution: oxidized, reduced and 2'-phospho-5'-AMP bound states, J Mol Biol 247 (1995) 125-145.

[17] I. Nogués, I. Pérez-Dorado, S. Frago, C. Bittel, S.G. Mayhew, C. Gómez-Moreno, J.A. Hermoso, M. Medina, N. Cortez, N. Carrillo, The ferredoxin-NADP(H) reductase from *Rhodobacter capsulatus*: molecular structure and catalytic mechanism, Biochemistry 44 (2005) 11730-11740.

[18] M. Ingelman, S. Ramaswamy, V. Niviere, M. Fontecave, H. Eklund, Crystal structure of NAD(P)H:flavin oxidoreductase from Escherichia coli, Biochemistry 38 (1999) 7040-7049.

[19] G. Lu, Y. Lindqvist, G. Schneider, U. Dwivedi, W. Campbell, Structural studies on corn nitrate reductase: refined structure of the cytochrome *b* reductase fragment at 2.5 Å, its ADP complex and an active-site mutant and modeling of the cytochrome *b* domain, J Mol Biol 248 (1995) 931-948.

[20] M.C. Bewley, C.C. Marohnic, M.J. Barber, The structure and biochemistry of NADH-dependent cytochrome b_5 reductase are now consistent, Biochemistry 40 (2001) 13574-13582.

[21] J. Tejero, J.R. Peregrina, M. Martínez-Júlvez, A. Gutiérrez, C. Gómez-Moreno, N.S. Scrutton, M. Medina, Catalytic mechanism of hydride transfer between $NADP^+$/H and ferredoxin-$NADP^+$ reductase from *Anabaena* PCC 7119, Arch. Biochem. Biophys. 459 (2007) 79-90.

[22] J.R. Peregrina, A. Sánchez-Azqueta, B. Herguedas, M. Martínez-Júlvez, M. Medina, Role of specific residues in coenzyme binding, charge-transfer complex formation, and catalysis in *Anabaena* ferredoxin-$NADP^+$ reductase, Biochim Biophys Acta 1797 (2010) 1638-1646.

[23] M. Medina, M. Martínez-Júlvez, J.K. Hurley, G. Tollin, C. Gómez-Moreno, Involvement of glutamic acid 301 in the catalytic mechanism of ferredoxin-$NADP^+$ reductase from *Anabaena* PCC 7119, Biochemistry 37 (1998) 2715-2728.

[24] I. Nogués, J. Tejero, J.K. Hurley, D. Paladini, S. Frago, G. Tollin, S.G. Mayhew, C. Gómez-Moreno, E.A. Ceccarelli, N. Carrillo, M. Medina, Role of the C-terminal tyrosine of ferredoxin-nicotinamide adenine dinucleotide phosphate reductase in the electron transfer processes with its protein partners ferredoxin and flavodoxin, Biochemistry 43 (2004) 6127-6137.

[25] M. Martínez-Júlvez, J. Hermoso, J.K. Hurley, T. Mayoral, J. Sanz-Aparicio, G. Tollin, C. Gómez-Moreno, M. Medina, Role of Arg100 and Arg264 from *Anabaena* PCC 7119 ferredoxin-$NADP^+$ reductase for optimal $NADP^+$ binding and electron transfer, Biochemistry 37 (1998a) 17680-17691.

[26] D.H. Paladini, M.A. Musumeci, N. Carrillo, E.A. Ceccarelli, Induced fit and equilibrium dynamics for high catalytic efficiency in ferredoxin-NADP(H) reductases, Biochemistry 48 (2009) 5760-5768.

[27] J.A. Hermoso, T. Mayoral, M. Faro, C. Gomez-Moreno, J. Sanz-Aparicio, M. Medina, Mechanism of coenzyme recognition and binding revealed by crystal structure analysis of ferredoxin-$NADP^+$ reductase complexed with $NADP^+$, J Mol Biol 319 (2002) 1133-1142.

[28] C.C. Correll, C.J. Batie, D.P. Ballou, M.L. Ludwig, Phthalate dioxygenase reductase: a modular structure for electron transfer from pyridine nucleotides to [2Fe-2S], Science 258 (1992) 1604-1610.

[29] H. Nishida, K. Inaka, M. Yamanaka, S. Kaida, K. Kobayashi, K. Miki, Crystal structure of NADH-cytochrome b_5 reductase from pig liver at 2.4 Å resolution, Biochemistry 34 (1995) 2763-2767.

[30] C.C. Marohnic, M.C. Bewley, M.J. Barber, Engineering and characterization of a NADPH-utilizing cytochrome b_5 reductase, Biochemistry 42 (2003) 11170-11182.

[31] M. Medina, A. Luquita, J. Tejero, J. Hermoso, T. Mayoral, J. Sanz-Aparicio, K. Grever, C. Gómez-Moreno, Probing the determinants of coenzyme specificity in ferredoxin-$NADP^+$ reductase by site-directed mutagenesis, J Biol Chem 276 (2001) 11902-11912.

[32] J. Tejero, M. Martínez-Júlvez, T. Mayoral, A. Luquita, J. Sanz-Aparicio, J.A. Hermoso, J.K. Hurley, G. Tollin, C. Gómez-Moreno, M. Medina, Involvement of the pyrophosphate and the 2'-phosphate binding regions of ferredoxin-$NADP^+$ reductase in coenzyme specificity, J. Biol. Chem. 278 (2003) 49203-49214.

[33] J.R. Peregrina, B. Herguedas, J.A. Hermoso, M. Martínez-Júlvez, M. Medina, Protein motifs involved in coenzyme interaction and enzymatic efficiency in *Anabaena* ferredoxin-$NADP^+$ reductase, Biochemistry 48 (2009) 3109-3119.

[34] A. Aliverti, T. Lubberstedt, G. Zanetti, R.G. Herrmann, B. Curti, Probing the role of lysine 116 and lysine 244 in the spinach ferredoxin-$NADP^+$ reductase by site-directed mutagenesis, J Biol Chem 266 (1991) 17760-17763.

[35] S. Baroni, V. Pandini, M.A. Vanoni, A. Aliverti, A single tyrosine hydroxyl group almost entirely controls the NADPH specificity of Plasmodium falciparum ferredoxin-$NADP^+$ reductase, Biochemistry 51 (2012) 3819-3826.

[36] L. Piubelli, A. Aliverti, A.K. Arakaki, N. Carrillo, E.A. Ceccarelli, P.A. Karplus, G. Zanetti, Competition between C-terminal tyrosine and nicotinamide modulates pyridine nucleotide affinity and specificity in plant ferredoxin-$NADP^+$ reductase, J Biol Chem 275 (2000) 10472-10476.

[37] J. Tejero, I. Pérez-Dorado, C. Maya, M. Martínez-Júlvez, J. Sanz-Aparicio, C. Gómez-Moreno, J.A. Hermoso, M. Medina, C-terminal tyrosine of ferredoxin-$NADP^+$ reductase in hydride transfer processes with $NAD(P)^+$/H, Biochemistry 44 (2005) 13477-13490.

[38] I. Lans, J.R. Peregrina, M. Medina, M. García-Viloca, A. González-Lafont, J.M. Lluch, Mechanism of the hydride transfer between *Anabaena* Tyr303Ser FNR_{rd}/FNR_{ox} and $NADP^+$/H. A combined pre-steady-state kinetic/ensemble-averaged transition-state theory with multidimensional tunneling study, J Phys Chem B 114 (2010) 3368-3379.

[39] J.R. Peregrina, I. Lans, M. Medina, The transient catalytically competent coenzyme allocation into the active site of *Anabaena* ferredoxin-$NADP^+$ reductase, Eur Biophys J (2012).

[40] P. Macheroux, UV-visible spectroscopy as a tool to study flavoproteins, Methods Mol Biol 131 (1999) 1-7.

[41] V. Rodríguez-Roldán, J.M. García-Heredia, J.A. Navarro, M. Hervás, B. De la Cerda, F.P. Molina-Heredia, M.A. De la Rosa, A comparative kinetic analysis of the reactivity of plant, horse, and human respiratory cytochrome *c* towards cytochrome *c* oxidase, Biochem Biophys Res Commun 346 (2006) 1108-1113.

[42] T.E. Meyer, Z.G. Zhao, M.A. Cusanovich, G. Tollin, Transient kinetics of electron transfer from a variety of *c*-type cytochromes to plastocyanin, Biochemistry 32 (1993) 4552-4559.

[43] S. Daff, An appraisal of multiple NADPH binding-site models proposed for cytochrome P450 reductase, NO synthase, and related diflavin reductase systems, Biochemistry 43 (2004) 3929-3932.

[44] W. Kabsch, Automatic processing of rotation diffraction data from crystals of initially unkown symmetry and cell constants, J Appl Cryst 26 (1993) 795-800.

[45] M.D. Winn, C.C. Ballard, K.D. Cowtan, E.J. Dodson, P. Emsley, P.R. Evans, R.M. Keegan, E.B. Krissinel, A.G. Leslie, A. McCoy, S.J. McNicholas, G.N. Murshudov, N.S. Pannu, E.A. Potterton, H.R. Powell, R.J. Read, A. Vagin, K.S. Wilson, Overview of the CCP4 suite and current developments, Acta Crystallogr D Biol Crystallogr 67 (2011) 235-242.

[46] A. Vagin, A. Teplyakov, MOLREP: an automated program for molecular replacement J. Appl. Cryst. 30 (1997) 1022-1025.

[47] G.N. Murshudov, A.A. Vagin, E.J. Dodson, Refinement of macromolecular structures by the maximum-likelihood method, Acta Crystallogr D Biol Crystallogr 53 (1997) 240-255.

[48] P. Emsley, B. Lohkamp, W.G. Scott, K. Cowtan, Features and development of Coot, Acta Crystallogr D Biol Crystallogr 66 (2010) 486-501.

[49] R.A. Laskowski, M.W. MacArthur, D.S. Moss, J.M. Thornton, PROCHECK: a program to check the stereochemical quality of protein structures, J. Appl. Cryst. 26 (1993) 283-291.

[50] I.W. Davis, A. Leaver-Fay, V.B. Chen, J.N. Block, G.J. Kapral, X. Wang, L.W. Murray, W.B. Arendall, 3rd, J. Snoeyink, J.S. Richardson, D.C. Richardson, MolProbity: all-atom contacts and structure validation for proteins and nucleic acids, Nucleic Acids Res 35 (2007) W375-383.

[51] J.K. Hurley, J.L. Schmeits, C. Genzor, C. Gómez-Moreno, G. Tollin, Charge reversal mutations in a conserved acidic patch in *Anabaena* ferredoxin can attenuate or enhance electron transfer to ferredoxin:$NADP^+$ reductase by altering protein/protein orientation within the intermediate complex, Arch Biochem Biophys 333 (1996) 243-250.

[52] S. Frago, I. Lans, J.A. Navarro, M. Hervás, D.E. Edmondson, M.A. De la Rosa, C. Gómez-Moreno, S.G. Mayhew, M. Medina, Dual role of FMN in flavodoxin function: electron transfer cofactor and modulation of the protein-protein interaction surface, Biochim Biophys Acta 1797 (2010) 262-271.

[53] M.A. Musumeci, H. Botti, A. Buschiazzo, E.A. Ceccarelli, Swapping FAD binding motifs between plastidic and bacterial ferredoxin-NADP(H) reductases, Biochemistry 50 (2011) 2111-2122.

[54] R. Morales, M.H. Charon, G. Kachalova, L. Serre, M. Medina, C. Gómez-Moreno, M. Frey, A redox-dependent interaction between two electron-transfer partners involved in photosynthesis, EMBO Rep 1 (2000) 271-276.

[55] J.K. Hurley, A.M. Weber-Main, M.T. Stankovich, M.M. Benning, J.B. Thoden, J.L. Vanhooke, H.M. Holden, Y.K. Chae, B. Xia, H. Cheng, J.L. Markley, M. Martínez-Júlvez, C. Gómez-Moreno, J.L. Schmeits, G. Tollin, Structure-function relationships in *Anabaena* ferredoxin: correlations between X-ray crystal structures, reduction potentials, and rate constants of electron transfer to ferredoxin:$NADP^+$ reductase for site-specific ferredoxin mutants, Biochemistry 36 (1997) 11100-11117.

[56] V.I. Dumit, T. Essigke, N. Cortez, G.M. Ullmann, Mechanistic insights into ferredoxin-NADP(H) reductase catalysis involving the conserved glutamate in the active site, J Mol Biol 397 (2010) 814-825.

[57] C.J. Batie, H. Kamin, Electron transfer by ferredoxin:$NADP^+$ reductase. Rapid-reaction evidence for participation of a ternary complex, J Biol Chem 259 (1984a) 11976-11985.

[58] C.J. Batie, H. Kamin, Ferredoxin:NADP+ oxidoreductase. Equilibria in binary and ternary complexes with NADP+ and ferredoxin, J Biol Chem 259 (1984b) 8832-8839.

[59] J. Sancho, C. Gómez-Moreno, Interaction of ferredoxin-$NADP^+$ reductase from *Anabaena* with its substrates, Arch Biochem Biophys 288 (1991) 231-238.

[60] A. Aliverti, R. Faber, C.M. Finnerty, C. Ferioli, V. Pandini, A. Negri, P.A. Karplus, G. Zanetti, Biochemical and crystallographic characterization of ferredoxin-$NADP^+$ reductase from nonphotosynthetic tissues, Biochemistry 40 (2001) 14501-14508.

[61] Y. Onda, T. Matsumura, Y. Kimata-Ariga, H. Sakakibara, T. Sugiyama, T. Hase, Differential interaction of maize root ferredoxin:$NADP^+$ oxidoreductase with photosynthetic and non-photosynthetic ferredoxin isoproteins, Plant Physiol 123 (2000) 1037-1045.

[62] C. Combet, M. Jambon, G. Deléage, C. Geourjon, Geno3D: automatic comparative molecular modelling of protein, Bioinformatics/computer Applications in The Biosciences 18 (2002) 213-214.

Figure 1

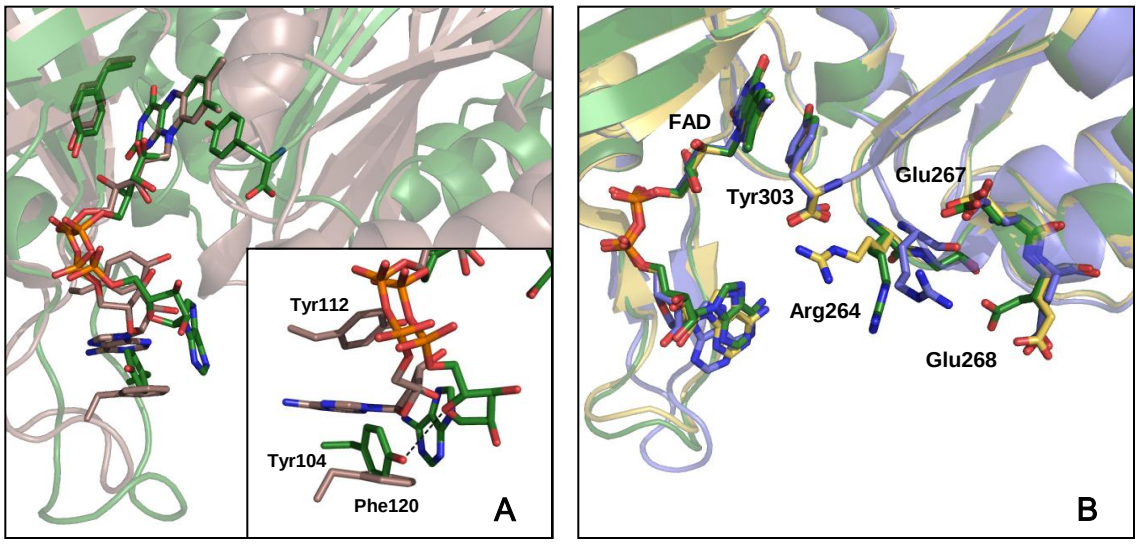

C

NADP-dependent	90	100	110	261	271	281	291	301
Anabaena PCC7119 FNR	VDDKTISLCVRQL**EY**KHPE**SG**ET			CGLRGM**EE**GIDAALSAAAAKEGVTWSDYQKDLKKAGRWHVETY				
Spirulina sp. FNR	VDDKTVSLCVRQL**EY**KHPE**TG**ET			CGLKGM**EG**GIDEGMSAAAGKFDVDWSDYQKELKKKHRWHVETY				
Synechococcus sp. FNR	EDNKTVSLCVRQL**EY**QDPE**SG**ET			CGLKGM**QP**PIDETFTAEAEKRGLNWEEMRRSMKKEHRWHVEVY				
Synechocystis sp. FNR	GDDKTVSLCVRQL**EY**QN-E**AG**ET			CGLKGM**EP**GIDEAFTALAEQNGKEWTTFQREMKKEHRWHVETY				
A. thaliana leaf FNR	GDSKTVSLCVKRL**VY**TN-D**GG**EI			CGLKGM**EK**GIDDIMVSLAAKDGIDWLEYKKQLKRSEQWNVEVY				
N. tabacum leaf FNR	GDSKTVSLCVKRL**VY**TN-D**KG**EE			CGLKGM**EQ**GIDEIMSALAERDGIVWADYKKQLKKAEQWNVEVY				
O. sativa leaf FNR	GDSKTVSLCVKRL**VY**TN-D**QG**EI			CGLKGM**EK**GIDDIMVSLAAKDGIDWADYKKQLKKGEQWNVEVY				
P. sativum leaf FNR	GDSKTVSLCVKRL**VY**TN-D**AG**EV			CGLKGM**EK**GIDDIMVSLAAKDGIDWIEYKRTLKKAEQWNVEVY				
S. oleracea FNR	GDAKSVSLCVKRL**IY**TN-D**AG**ET			CGLKGM**EK**GIDDIMVSLAAAEGIDWIEYKRQLKKAEQWNVEVY				
A. thaliana root FNR	FDGKTASLCVRRA**IY**YDPE**TG**KE			CGLKGM**MP**GIQDTLKRVAEERGESWEQKLTQLRKNKQWHVEVY				
N. tabacum root FNR	FDGKTASLCVRRA**VY**YDPE**TG**KE			CGLKGM**MP**GIQDTLKRVAERRGESWEQKLSQLKKNKQWHVEVY				
O. sativa root FNR	FDGRTTSLCVRRA**VY**YDPE**TG**KE			CGLKGM**MP**GIQDTLKKVAEQRGESWEQKLSQLKKNKQWHVEVY				
P. sativum root FNR	FDGKTASLCVRRA**VY**YDPV**TG**KE			CGLRGM**MP**GIQETLKRVAEKRGESWEEKLSQLKKNKQWHVEVY				
L. interrogans FNR	MKEDNIEFIIKRD**NI**YD-E**NG**NI			GGPKGM**EK**GVIEEIQKISGNTG-TYEEFKHHLEGAHQLFVETY				

NAD-dependent			
Z. mays NR	--IGHFDLLVKV**YF**KNEHPK**FP**N		CGPPPMIQFAISPNLEKMKYDMANSFVVF
R. norvegicus cb5R	--KGFVDLVVKV**YF**KDTHPK**FP**A		CGPPPMIQFACLPNLERVGHPKERCFTF
S. scrofa cb5R	--KGFVDLVIKV**YF**KDTHPK**FP**A		CGPPPMIQYACLPNLERVGHPKERCFAF
B. taurus cb5R	--QGYVDLVIKV**YL**KGVHPK**FP**E		CGPPPMVQLACHPSLDKLGYSPKMRFTY

Figure 2

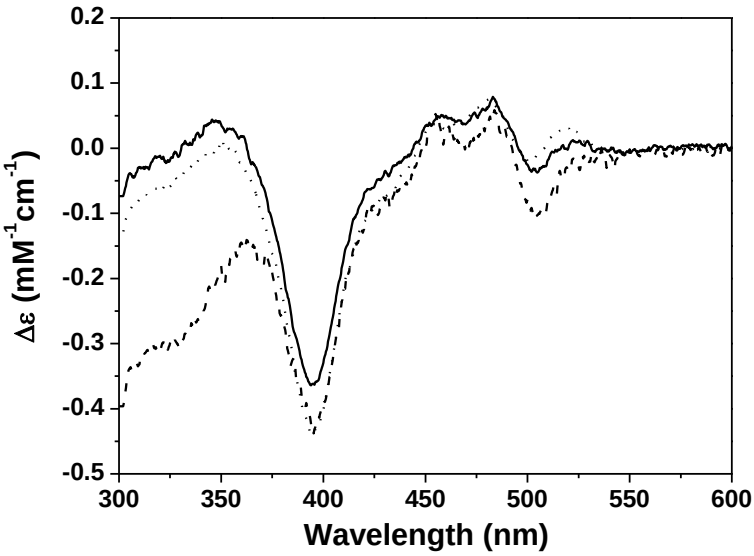
0.2
0.1
0.0
-0.1
-0.2
-0.3
-0.4
-0.5
Δε (mM-1cm-1)
300
350
400
450
500
550
600
Wavelength (nm)

Figure 3

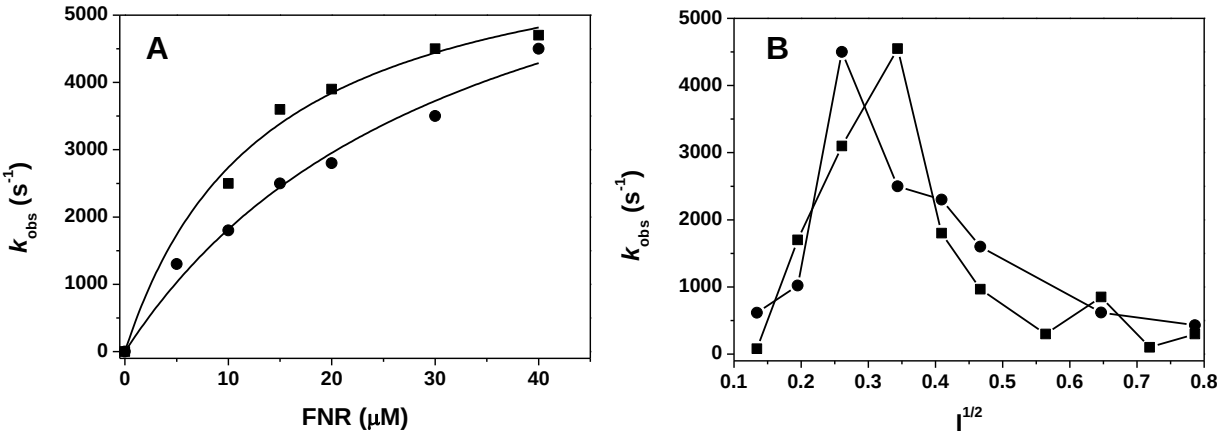
A
B
k_{obs} (s^{-1})
FNR (μM)
$I^{1/2}$
0
1000
2000
3000
4000
5000
0
10
20
30
40
0.1
0.2
0.3
0.4
0.5
0.6
0.7
0.8

Figure 4

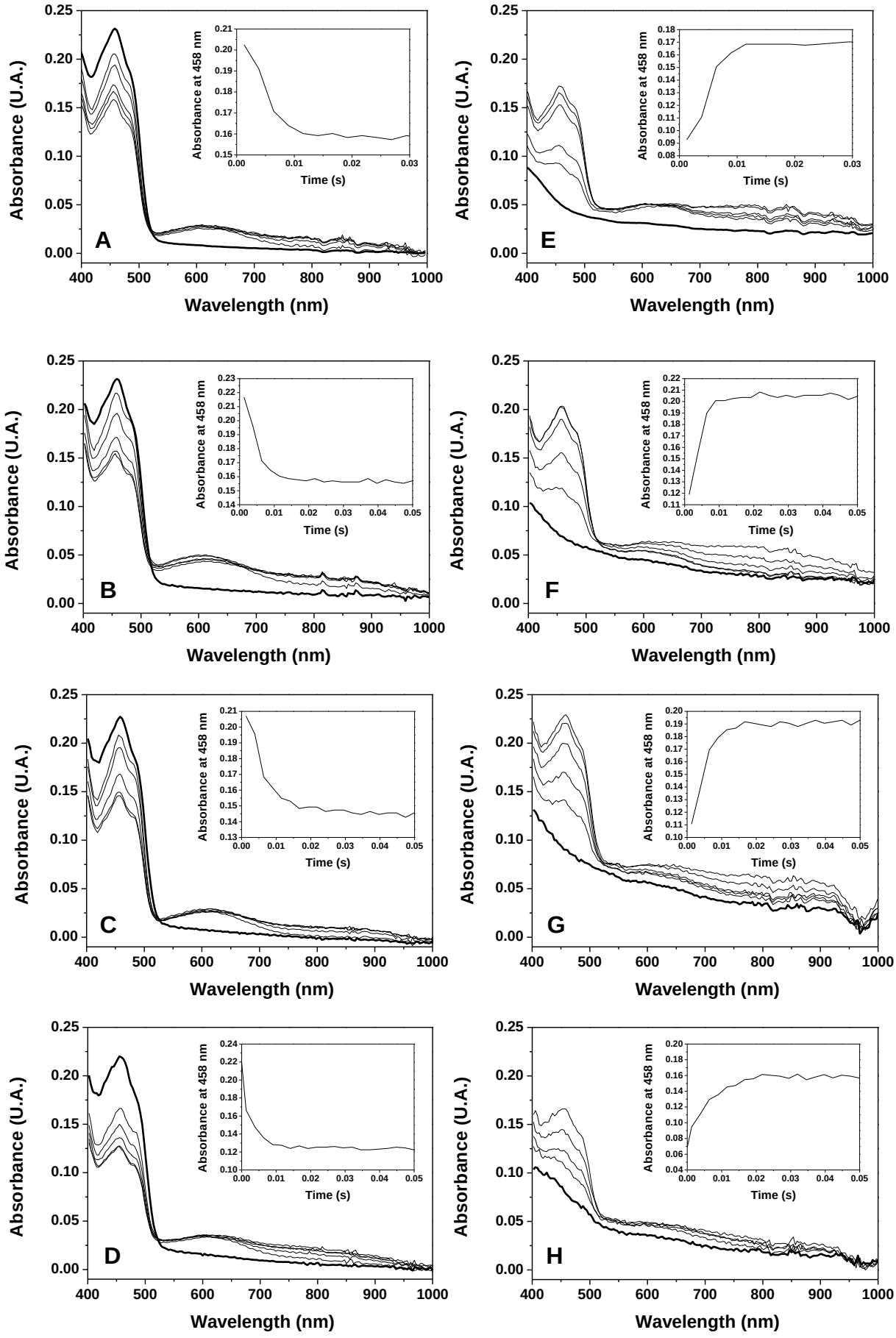
A
B
C
D
E
F
G
H
Absorbance (U.A.)
Wavelength (nm)
Absorbance at 458 nm
Time (s)

Figure 5

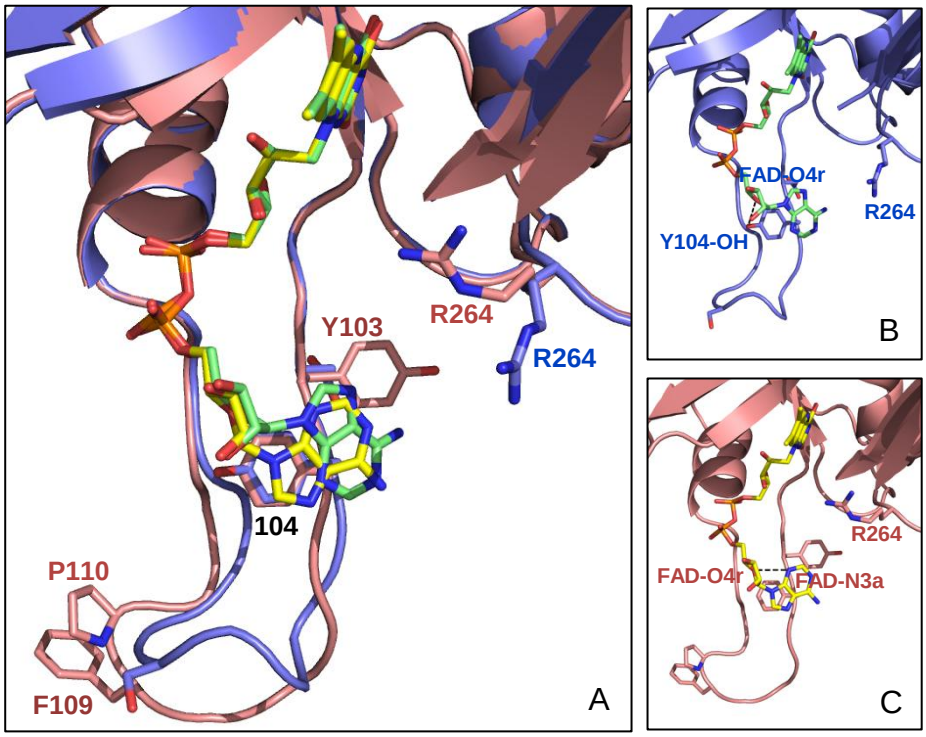
Y103
R264
R264
104
P110
F109
A
FAD-O4r
R264
Y104-OH
B
R264
FAD-O4r
FAD-N3a
C

Figure 6

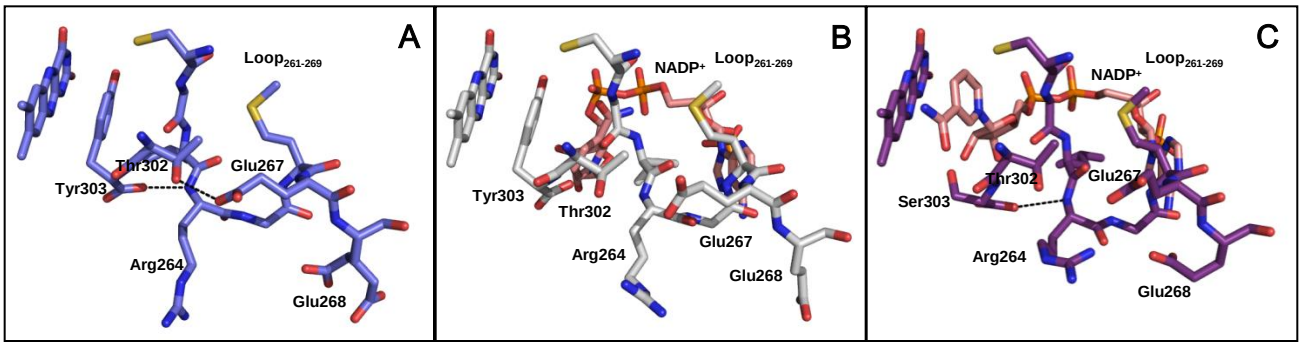
A
Loop261-269
Thr302
Glu267
Tyr303
Arg264
Glu268
B
NADP+
Loop261-269
Tyr303
Thr302
Arg264
Glu267
Glu268
C
NADP+
Loop261-269
Thr302
Glu267
Ser303
Arg264
Glu268

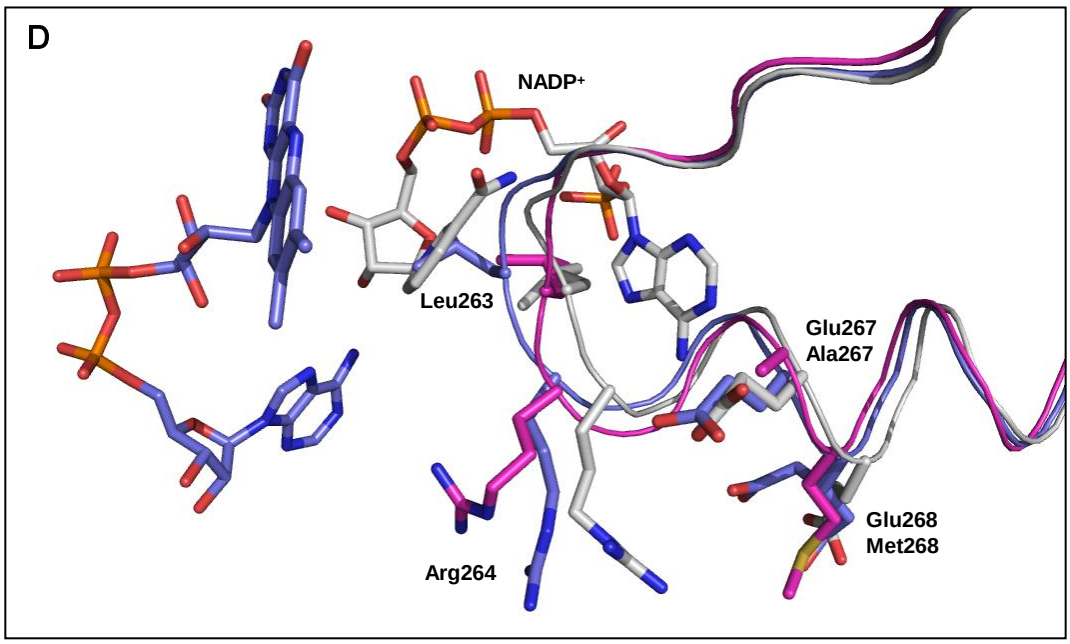
D
NADP+
Leu263
Glu267
Ala267
Glu268
Met268
Arg264

SUPPLEMENTARY INFORMATION

External loops at the ferredoxin-NADP$^+$ reductase protein-partner binding cavity contribute to substrates allocation

Ana Sánchez-Azqueta[1], Marta Martínez-Júlvez[1], Manuel Hervás[2], José A. Navarro[2], and Milagros Medina[1]

[1]*Departamento de Bioquímica y Biología Molecular y Celular, Facultad de Ciencias, and Institute of Biocomputation and Physics of Complex Systems (BIFI)-Joint Unit BIFI-IQFR (CSIC), Universidad de Zaragoza, Zaragoza, Spain.*
[2]*Instituto de Bioquímica Vegetal y Fotosíntesis, cicCartuja, Universidad de Sevilla & CSIC, Sevilla, Spain.*

Table SP1. Structure determination and statistics for E103Y/Y104F/S109F/G110P *An*FNR

Data collection statistics	
Space group	$P6_5$
Unit cell parameters	
a, Å	87.41
b, Å	87.41
c, Å	96.45
Wavelength, Å	0.97626
Resolution, Å	43.71-1.70 (1.79-1.70)
No. of unique reflections	45911
Redundancy	9.3 (9.2)
Completeness, %	99.8 (100)
Mn(I)/sd	16.1 (5.7)
R_{merge} [a]	0.077 (0.268)
Refinement statistics	
Resolution range, Å	43.71-1.70
Protein non-hydrogen atoms	2354
Ligand non-hydrogen atoms	64
Solvent non-hydrogen atoms	305
R_{work} (%)	17.5
R_{free} [b] (%)	20.5
r.m.s.d. bond lenght, Å	0.006
r.m.s.d. bond angles, °	1.293
Average B-factor, $Å^2$	20.8

Values in parentheses correspond to the highest resolution shell.
[a] $Rsym = \Sigma| I - I_{av} |/ \Sigma I$, where the summation is over symmetry equivalent reflections.
[b] R calculated for 7% of data excluded from the refinement.

Figure SM1

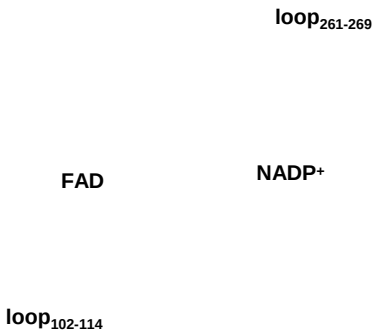

Figure SM1. Disposition of loops $loop_{102-114}$ and $loop_{261-269}$ in a theoretical Fd:FNR:$NADP^+$ ternary complex from *Anabaena*. The model has been constructed by structural alignment of the crystallographic structures of the *An*Fd:*An*FNR (PDB ID 1EWY) and *An*FNR:$NADP^+$ complexes (C-II, PDB ID 1GJR). FNR is shown with the FAD-binding domain in yellow and the $NADP^+$/H-binding domain in blue, while the loops analyzed in this work, $loop_{102-114}$ and $loop_{261-269,}$ are highlighted in brawn and dark blue, respectively. Fd is shown in green with its iron-sulfur cluster in spheres. FAD and $NADP^+$ are shown in sticks and CPK coloured with carbons in grey and pink, respectively.

Figure SM2

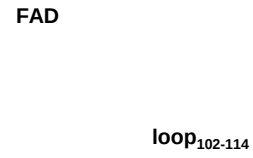

Figure SM2. **Conformational changes induced in the loop$_{102-104}$ by the mutations.** Superimposition of the crystallographic structures of wild type *An*FNR, free (PDB ID 1QUE, grey) and in complex with *An*Fd (PDB ID 1EWY, *An*Fd in green, *An*FNR in blue), and that of E103Y/Y104F/S109F/G110P *An*FNR (PDB ID 4C43, in pink). The FAD molecule corresponding to the 1QUE structure is shown in sticks with carbons in grey. The *An*Fd iron sulphur cluster is shown as sticks.

Figure SM3

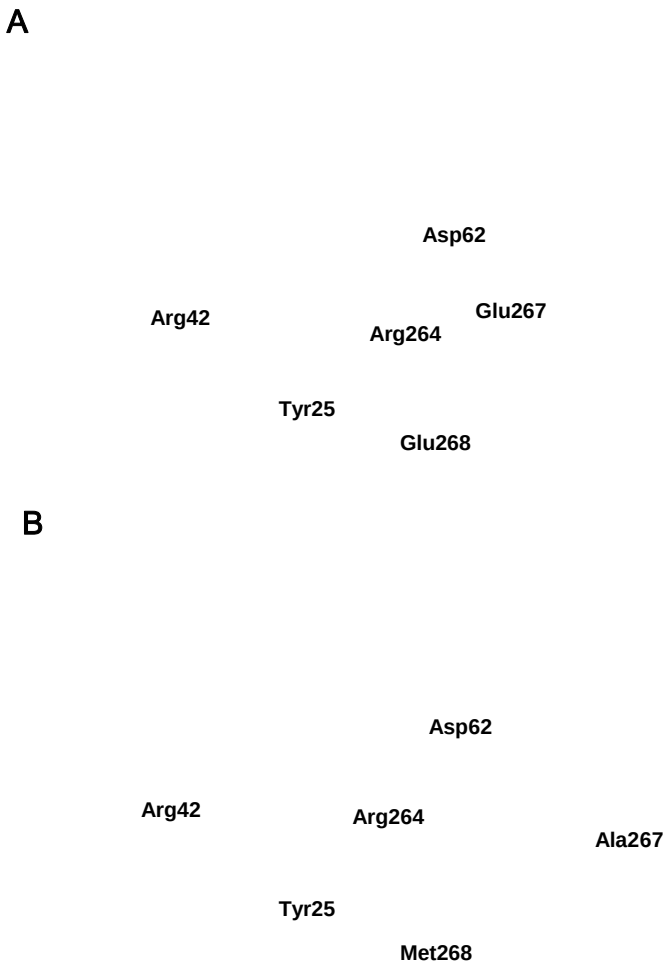

Figure SM3. The interaction of FNR with Fd. (A) Crystal structure of the *An*FNR:*An*Fd complex (PDB 1EWY). **(B)** Predicted structural model for a complex of *An*Fd with E267A/E268M *An*FNR. The E267A/E268M *An*FNR model was generated using the 1EWY structure as template and the Geno3D software. *An*Fd and *An*FNR are represented in green and blue, respectively, and E267A/E268M *An*FNR in pink. The Arg264-Tyr25 and Glu267-Asp62 connections are not anymore expected in the model for the mutant complex.